Gaborheometry: Applications of the discrete Gabor transform for time resolved oscillatory rheometry

Joshua David John Rathinaraj and Gareth H. McKinley

Citation: Journal of Rheology **67**, 479 (2023); doi: 10.1122/8.0000549
View online: https://doi.org/10.1122/8.0000549
View Table of Contents: https://sor.scitation.org/toc/jor/67/2
Published by the The Society of Rheology

Gaborheometry: Applications of the discrete Gabor transform for time resolved oscillatory rheometry

Joshua David John Rathinaraj[a] and Gareth H. McKinley[b]

Hatsopoulos Microfluids Laboratory, Department of Mechanical Engineering, Massachusetts Institute of Technology, Cambridge, Massachusetts 02139

(Received 13 August 2022; final revision received 18 November 2022; published 3 February 2023)

Abstract

Oscillatory rheometric techniques such as small amplitude oscillatory shear (SAOS) and, more recently, medium amplitude oscillatory shear and large amplitude oscillatory shear (LAOS) are widely used for rheological characterization of the viscoelastic properties of complex fluids. However, in a time-evolving or mutating material, the build-up or breakdown of microstructure is commonly both time- and shear-rate (or shear-stress) dependent, and thixotropic phenomena are observed in many complex fluids including drilling fluids, biopolymer gels, and many food products. Conventional applications of Fourier transforms for analyzing oscillatory data assume the signals are time-translation invariant, which constrains the mutation number of the material to be extremely small. This constraint makes it difficult to accurately study shear-induced microstructural changes in thixotropic and gelling materials, and it is becoming increasingly important to develop more advanced signal processing techniques capable of robustly extracting time-resolved frequency information from oscillatory data. In this work, we explore applications of the Gabor transform (a short-time Fourier transform combined with a Gaussian window), for providing optimal joint time-frequency resolution of a mutating material's viscoelastic properties. First, we show using simple analytic models and measurements on a bentonite clay that the Gabor transform enables us to accurately measure rapid changes in both the storage and/or loss modulus with time as well as extract a characteristic thixotropic/aging time scale for the material. Second, using the Gabor transform we demonstrate the extraction of useful viscoelastic data from the initial transient response following the inception of oscillatory flow. Finally, we consider extension of the Gabor transform to nonlinear oscillatory deformations using an amplitude-modulated input strain signal, in order to track the evolution of the Fourier–Tschebyshev coefficients of thixotropic fluids at a specified deformation frequency. We refer to the resulting test protocol as Gaborheometry (Gabor-transformed oscillatory shear rheometry). This unconventional, but easily implemented, rheometric approach facilitates both SAOS and LAOS studies of time-evolving materials, reducing the number of required experiments and the data postprocessing time significantly. https://doi.org/10.1122/8.0000549

I. INTRODUCTION

There have been significant advances in the field of signal processing in the last 50 years whose utilization spans a variety of engineering and research applications including acoustics, image processing, astronomy, data transmission, speech recognition, as well as medical imaging such as CAT scans and MRI [1–7]. These advanced signal processing techniques have, until recently, been under-utilized in the field of rheometry and soft matter. However, in recent years, there has been a significant trend in developing signal processing techniques relevant to soft material characterization such as large amplitude oscillatory shear (LAOS) [8–16], medium amplitude oscillatory shear (MAOS) [17,18], the sequence of physical processes (SPPs) [19,20] framework, and medium amplitude parallel superposition (MAPS) [21,22]. These techniques help in quantifying the viscoelastic material properties and physically meaningful information of an unknown material, which paves the way for understanding the flow behavior of the material at different stresses or strain states. For viscoelastic materials, the resulting rheological measures are a function of the frequency and strain amplitude of the material deformation and facilitate detailed characterization of materials for a range of applications in consumer industries, automotive sectors, and the oil and gas industries [23,24]. However, the signal processing algorithms used to analyze these oscillatory techniques, including conventional small amplitude oscillatory shear (SAOS), most commonly utilize the discrete Fourier transform (DFT), which does not intrinsically provide any time resolution by itself. This makes it difficult to characterize mutating materials, which are both time and shear-rate or shear-stress dependent.

There are numerous microstructural mechanisms that are responsible for the time-evolving or "mutating" nature of viscoelastic properties in complex fluids. For example, in metal-ion crosslinked polymers, the metal-ion coordinate bonds can be reversible [25,26]. This results in the build-up or recovery of structural features over time when breakdown of the microstructure is initiated by large deformations at high shear rates or stresses. Shear-induced microstructural build-up and breakdown (not necessarily by reversible covalent bonds) over time is reflected in terms of the dependence of viscoelastic properties not just on the imposed test frequency but also on the elapsed time or waiting time since the system was prepared or loaded into the measurement device. This phenomenon is common in many complex fluids, and such systems (which do not satisfy time translation invariance) are

[a]Electronic mail: joshuajr@mit.edu
[b]Author to whom correspondence should be addressed; electronic mail: gareth@mit.edu

widely characterized or collectively referred to as thixotropic materials [27–30]. In soft glassy materials, there is no need for a preceeding shear or large deformations to induce structural build-up. These materials are out of thermodynamic equilibrium and show time-dependent slowing down of their relaxation dynamics with age [31–37]. The thermally driven mobility of the microscopic constituents induces slow inexorable structural evolution with time, resulting in formation of progressively more stable structures that reduce the overall free energy of the system. This process of structural evolution with time observed in soft glassy materials is also known as physical aging [38–44]. In the process of physical aging, the elastic modulus and relaxation time characterizing the material viscoelasticity typically increase monotonically with waiting time.

To quantify the rate of evolution in such mutating materials, Winter *et al.* [45] introduced a dimensionless number called the mutation number Mu_G as a measure to characterize the rate of change in the relevant property of the system within the given experimental time. Here, G indicates the generic property of interest and Mu is defined as the ratio between the mutation time λ_{Mu} and the experimental time Δt required to measure the material property of interest [45]. The mutation time λ_{Mu} is defined as the characteristic time constant for the change of material,

$$\lambda_{Mu} = \frac{G}{dG/dt} = \left|\frac{d\ln G}{dt}\right|^{-1}. \tag{1}$$

The relevant experimental time Δt_{exp} for an oscillatory shear experiment which takes a single cycle to complete is $\Delta t_{\text{exp}} = 2\pi/\omega$. Therefore, the mutation number can be written as

$$Mu_G = \frac{\Delta t_{\text{exp}}}{\lambda_{Mu}} = \frac{2\pi}{\omega}\left|\frac{d\ln G}{dt}\right|. \tag{2}$$

Winter and Mours show that in order to obtain accurate measurements, the property G should not change significantly within the duration of the experiment and careful experimental tests suggest the criterion $Mu_G \leq 0.15$ [46].

In Fig. 1, we reproduce data from [47] which shows the time-dependent evolution of the elastic modulus of several representative soft, physically aging materials. The three materials shown in Fig. 1 are an unspecified gel, a food suspension (mustard), and a bentonite clay, which is commonly used in the drilling industry. It is clear that the bentonite sample has the highest mutation number among the three systems. Satisfying the criterion $Mu_G \leq 0.15$ can be challenging for such rapidly mutating systems. The time dependency of the material properties can be observed in the steady flow curves as well, as indicated by the "thixotropic loop" test protocol shown in Fig. 2. Each flow curve can be well described by the Herschel–Bulkley model $\sigma = \sigma_y + k\dot{\gamma}^n$ but a systematic increase of the yield stress $\sigma_y(t)$ is observed with the elapsed measuring time. Such thixotropic or hysteretic characteristics are also reflected in small amplitude oscillatory measurements which are used to measure the frequency-dependent complex modulus of the material [48]. Exploring the temporal evolution of the viscoelastic properties of mutating materials provides deeper insight into the rheological behavior and characteristics of thixotropic viscoelastic systems. For such mutating materials, Geri *et al.* introduced the optimally windowed chirp (OWCh) protocol which makes use of a frequency modulated exponential chirp signal in conjunction with a Tukey window. The resulting signal waveform can supplant standard SAOS techniques to enable rapid determination of the frequency response of viscoelastic materials in the linear regime [49,50]. This technique reduces the experimental time Δt_{exp} required to perform a frequency sweep and results in a substantial reduction in the mutation number Mu_G. This protocol has been used with a range of time-evolving systems to obtain the frequency response

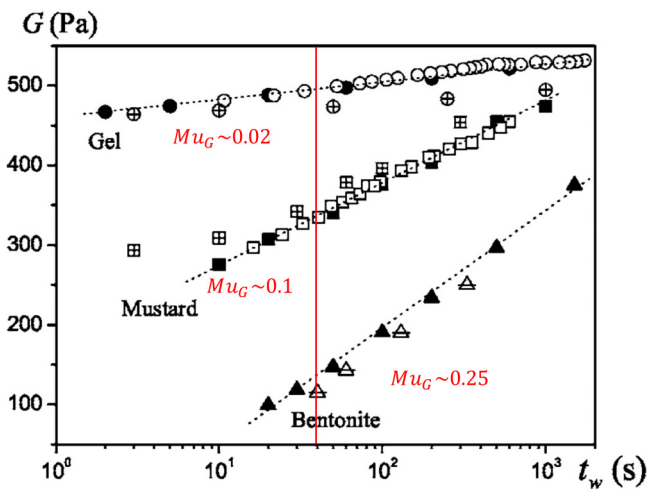

FIG. 1. Time-dependent evolution of the elastic modulus for various thixotropic mutating materials. Reproduced with permission from Coussot *et al.*, J. Rheol. **50**, 975–994 (2006). Copyright 2006, AIP Publishing LLC. Here, t_w represents the elapsed or waiting time (after the initial preshear) at which the small amplitude oscillatory deformation is imposed to obtain the reported moduli data. The steeper slope for the bentonite data indicates a higher mutation number Mu_G than the samples labeled gel and mustard.

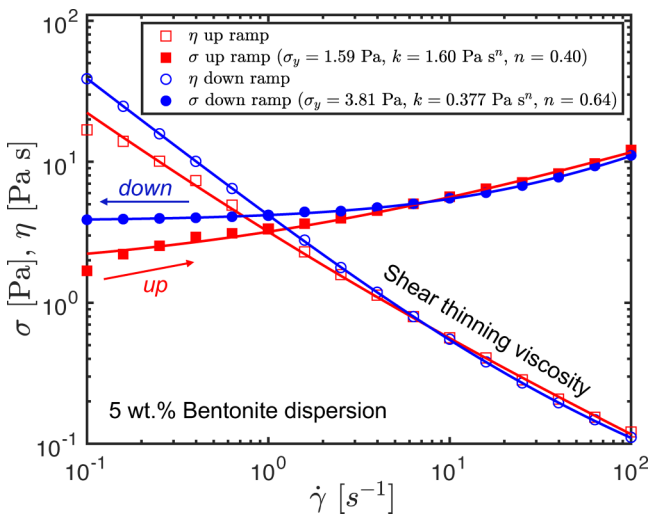

FIG. 2. Time dependent evolution in the steady shear viscosity and shear stress for a 5% bentonite dispersion in de-ionized water. Blue color indicates the data for which the shear rate is increased from $\dot{\gamma} = 0.1$ to $100\,\text{s}^{-1}$ in five equally exponentially spaced steps per decade. Red color indicates the data for which the shear rate is decreased from $\dot{\gamma} = 100$ to $0.1\,\text{s}^{-1}$. The total elapsed time of sweep in one direction is 1800 s.

characteristics of a material at a given instant of time for a range of frequencies [51–53]. There have also been developments on evaluating the linear viscoelastic complex modulus from the full information obtained rheometrically in step strain experiments, and this can again reduce the experimental test time Δt_{exp} and, thus, the mutation number Mu_G [54]. However, for rapidly mutating materials, even the usage of the OWCh techniques can be challenging since it can be difficult to satisfy the criteria $Mu_G \leq 0.15$ [55].

A desirable feature of any new advanced signal processing technique would be to enable both time and frequency resolution of rapidly mutating materials, which are of high interest to various industrial and biomedical applications. To this end, we consider here the Gabor transform for analysis of rheometric data. This is a special case of the short time fourier transform (STFT) and enables determination (within constraints discussed later) of both the time and frequency content of a signal from oscillatory experiments. The Gabor transform uses a temporally localized Gaussian function as a window in conjunction with a Fourier transform to provide both time and frequency resolution. The use of a Gaussian windowing function helps facilitate derivation of analytical results on the errors incurred and helps us to understand the details of the process theoretically. The Gaussian window has been proven to have the minimum time-frequency uncertainty [56,57] of available window functions providing a strong case to use this special case of the STFT for rheometric applications.

We start by briefly reviewing the DFT and its limitations. Then, we introduce the Gabor transform and the computational details required, such as selection of window length and amplitude correction, to enable its use for quantitative rheometry. We first demonstrate use of the Gabor transform to resolve the time-dependent complex modulus in a simple aging Kelvin– Voigt model and then proceed to use the algorithm developed to extract the time-dependent complex modulus of an aging 5 wt. % bentonite dispersion. We also discuss in detail two other applications of the Gabor transform in rheometry: (i) extracting the long time steady-state frequency response (also known as the alternance state) as well as the transient response accurately from the initial oscillatory data recorded following the inception of oscillatory shear. This helps us to extract quantitative data from short duration experiments and reduces the need to wait long periods for the initial viscoelastic transient response to subside; (ii) accurately extracting and monitoring the evolution of the nonlinear Fourier–Tschebyshev coefficients in LAOS with increasing strain (or stress) amplitude at a specified deformation frequency using an amplitude-modulated (AM) signal. This latter application streamlines the implementation of LAOS tests by reducing the number of experiments required and the data postprocessing times that are required to obtain the nonlinear Fourier–Tschebyshev coefficients characterizing viscous and elastic nonlinearities. We refer to the use of the discrete Gabor transform for rheometric applications as *Gaborheometry*. Finally, we discuss the importance of Heisenberg's time-frequency uncertainty principle [58,59] in implementing the Gabor transform, which provides guidance in optimizing the trade-off between selecting time and frequency resolution and its importance in designing convenient and robust experimental protocols for Gaborheometry.

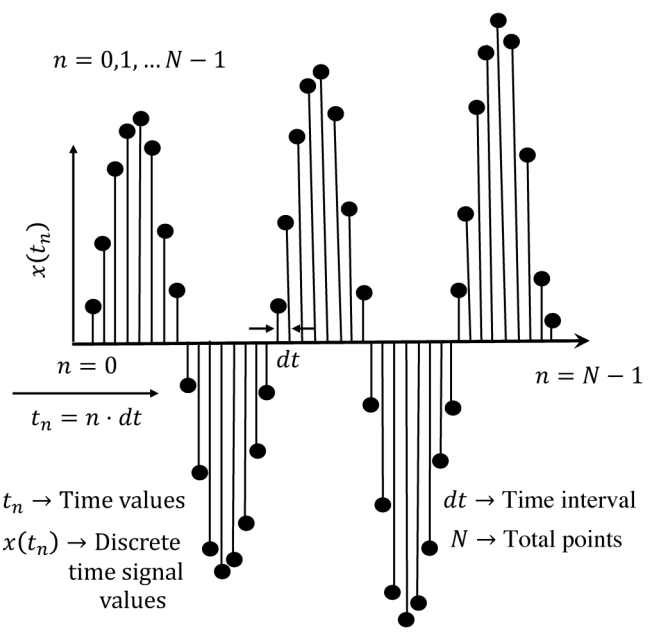

FIG. 3. A typical digital signal from a rheometer is composed of N total points with a time interval dt. $x(t_n)$ corresponds to the sampled digital signal at $x(n \cdot dt)$ where $n \in 0, 1, 2, \ldots, N-1$.

II. THE DISCRETE FOURIER TRANSFORM IN RHEOMETRY

A. Introduction to the DFT

The complex modulus of a linear viscoelastic material can be defined for a periodic small amplitude oscillatory shearing deformation by

$$G^*(\omega) = G'(\omega) + iG''(\omega) = \frac{\tilde{\sigma}(\omega)}{\tilde{\gamma}(\omega)}, \tag{3}$$

where $\tilde{\sigma}(\omega)$ is the Fourier transform (FT) of the stress signal and $\tilde{\gamma}(\omega)$ is the Fourier transform of the strain signal [60]. The real part of the complex modulus is the storage modulus, and the imaginary part is termed the loss modulus. In practice, the Fourier transform operation is computed using the DFT algorithm. The key parameters for a time and frequency-varying signal are shown systematically in Fig. 3. The discrete Fourier transform of a digitally sampled time series $x(t)$ (with N samples) considers the entire record length and is defined as

$$\tilde{x}_{DFT}(\omega_k) = \sum_{n=0}^{N-1} x(t_n) e^{-i\omega_k t_n} \qquad k = 0, 1, 2, \ldots, N-1 \tag{4}$$

where $x(t_n)$ is the input signal amplitude at each time t_n, N is the total number of points present in the digital signal or the number of time samples, dt is the time sampling interval, and $t_n = n \cdot dt$ is the time value of the nth sampling instant. The total duration of the signal is $T = (N-1)dt$. The output consists of complex information samples at discrete frequencies ω_k between $\omega = 0$ and $\omega = 2\pi/dt$. The complex value of

$\tilde{x}_{\mathrm{DFT}}(\omega_k)$, which is the DFT at frequency $\omega = \omega_k$, is a measure of the amplitude and phase of the information present in the input signal $x(t)$ at that frequency where $\omega_k = 2\pi k/(N \cdot dt)$ [61]. However, the second half of the vector in frequency the domain does not contain new information ($n \in N/2, \ldots, N-1$). Therefore, only $N/2$ (plus a DC term) frequency samples with unique (complex) information are obtained in the frequency domain from N discrete time samples. These different parameters are depicted schematically in Fig. 3.

B. Limitations of DFT: No time resolution and assumption of time translation invariance (TTI)

Computation of the discrete Fourier transform at a frequency ω_k considers the entire sampled time signal $x(t_n)$ ($n = 0, 1, \ldots, N-1$) in order to calculate the amplitudes of the different frequency components present in the time signal. Time-resolved frequency information at an arbitrary time t_n is not obtainable from Eq. (4) using a discrete Fourier transform. To illustrate this, in Fig. 4, we show a time signal comprised of two distinct frequencies. The signal is constructed by the following stepwise change in frequency:

$$x(t) = \begin{cases} \sin(1t), & t < 20\pi \text{ s}, \\ \sin(5t), & t \geq 20\pi \text{ s}. \end{cases} \tag{5}$$

The discrete Fourier transform of the resulting signal constructed from Eq. (5) is also shown in Fig. 4. As expected, the Fourier transform correctly gives information about the two different frequencies (1 and 5 rad/s) present in the time signal; however, time-resolved frequency information for locating *when* the peaks at $\omega = 1$ rad/s and $\omega = 5$ rad/s are present in the original signal is not clearly indicated. The small amplitude oscillations seen in Fig. 4 are known as Fresnel ripples and indicate that the signal is not infinitely periodic. They represent the step discontinuity of the discrete frequency components in the signal. However, reconstructing the fact that the discontinuity occurred at a time $t_i = 20\pi$ is not evident.

The second limitation of the discrete Fourier transform is the assumption of TTI in the harmonic content of the signal. To illustrate this limitation, we construct a sinusoidal signal with a strictly increasing amplitude

$$x(t) = 0.1t \sin(\omega_i t), \tag{6}$$

where $\omega_i = 1$ rad/s. The resulting time signal is shown in Fig. 5(a) by the orange solid line and the discrete Fourier transform of Eq. (6) is plotted in Fig. 5(b). The corresponding time invariant sinusoid with amplitude of $0.1T/2$ (T being the duration of the time signal) and fixed frequency of ω_i is shown in Fig. 5(a) by the blue curve. In contrast to the DFT of a time-invariant sinusoid, the DFT of the time signal in Eq. (6) is nonzero even at frequencies $\omega \neq \omega_i$,

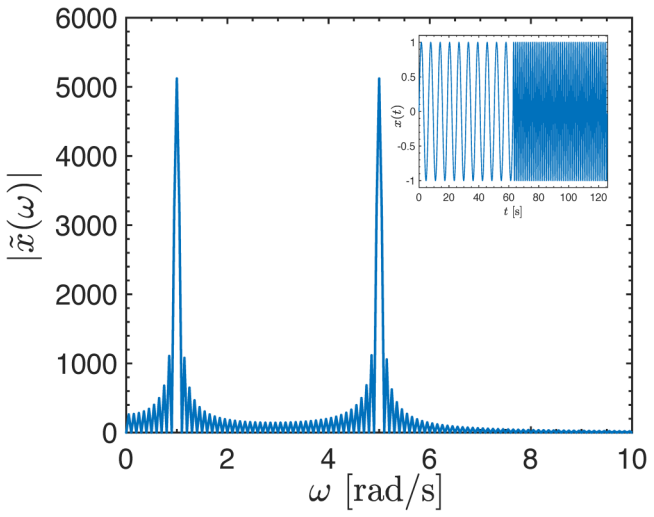

FIG. 4. A discrete Fourier transform (DFT) ($N = 10\,240$, $Ndt = 40\pi$ s) showing the frequency content of the signal constructed according to Eq. (5). In the inset, we show the original time series. The ripples observed in the frequency spectrum around the two primary peaks (located at $\omega = 1$ and $\omega = 5$ rad/s) arise because of the sharp discontinuity and finite periodicity of each part of the composite time signal.

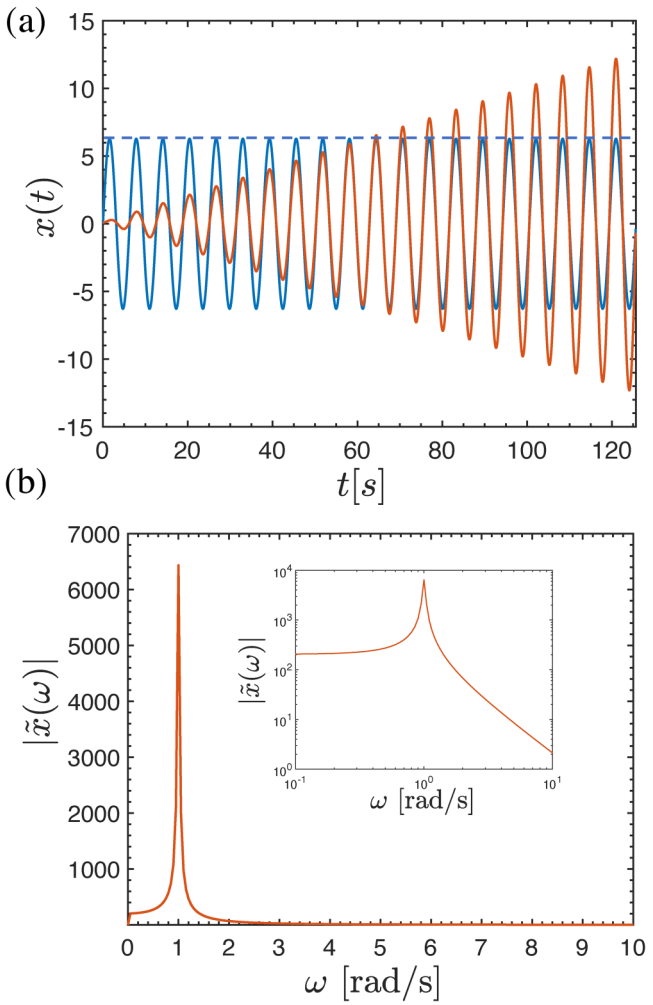

FIG. 5. (a) The orange solid line represents a sinusoidal signal whose amplitude increases linearly with time according to Eq. (6). The blue solid line represents the signal reconstructed just from the peak value of the frequency spectrum of Eq. (6). The total number of points $N = 20\,480$ and the duration of the time signal is $Ndt = 40\pi$ s. (b) The plot shows the frequency spectrum of the time signal in Eq. (6). The nonzero contributions observed in the inset figure distinct from the peak frequency $\omega = 1$ rad/s are due to the time varying amplitude of the input sinusoidal signal $x(t) = 0.1t \sin(t)$.

where $\omega_i = 1$ rad/s for our example. This can be more clearly visualized by using a logarithmic scaling, as shown in the inset of Fig. 5(b). The peak value of the discrete transform at $\tilde{x}(\omega = \omega_i)$ in Fig. 5(b) equals the value of the DFT at $\omega = \omega_i$ of the time-invariant sinusoidal signal with a frequency of ω_i and amplitude of $0.1T/2$. For thixotropic and aging materials, in which the output signal corresponds to the measured stress response to a constant amplitude sinusoidal strain input, using just the numerical value of the DFT peak located at the frequency of input signal in order to calculate the material property will result in an estimate of the mean value of G^* over the entire duration of the experiment but does not provide us with the dependence of the complex moduli on time.

C. Piece-wise analysis

The most common technique employed for thixotropic and aging materials in which the modulus is both time- and frequency-varying is a piece-wise analysis. The output signal is broken into a number of discrete consecutive segments. Each piece-wise signal corresponds to a particular age time and is processed separately by discrete Fourier transform to monitor the time-dependency of the viscoelastic properties of aging and thixotropic materials. For rapidly mutating materials, this piece-wise decomposition makes it difficult to obtain accurate results [45].

As we have attempted to show from these illustrative examples, it is important to develop more advanced signal processing techniques which can accommodate time- and frequency-varying inputs that do not require time translation invariance in order to extract information about temporal variations in the complex modulus $G^*(\omega, t)$ for thixotropic and aging materials. Recognizing the advancements in other multifrequency data-rich rheometric techniques such as OWCh and MAPS, we now seek a time-resolved protocol which can capture and separate both time and frequency information for mutating soft material samples.

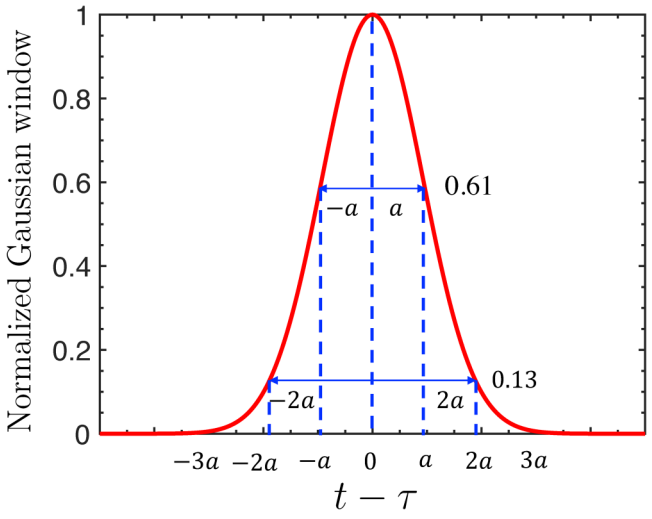

FIG. 6. The variation in a normalized Gaussian window $g(t-\tau)/g(0)$ given by Eq. (9). The parameter a of this Gaussian function controls the window width. The normalized value of the window at $t-\tau = a$ is $g(a)/g(0) = 0.61$ and at $t-\tau = 2a$ has decreased to $g(2a)/g(0) = 0.13$.

III. GABOR TRANSFORM

A. Introduction to the Gabor transform

The STFT is used to obtain both time and frequency resolution of a time-varying input signal. In a STFT, the temporal signal $x(t)$ is first multiplied by a window function $w(t-\tau)$ and then a Fourier transform is taken [62],

$$\tilde{x}(\tau, \omega) = \int_{-\infty}^{\infty} x(t) w(t-\tau) e^{-i\omega t} dt. \tag{7}$$

Here, τ and ω are the time and frequency of interest. The window function $w(t-\tau)$ localizes the time information provided by the STFT.

The Gabor transform is a special case of the STFT in which the window function is given by a Gaussian function [56]. The Gaussian function $g(t-\tau)$ is multiplied into the signal $x(t)$ and then the Fourier transform is computed to provide both time (τ) and frequency (ω) resolution. The Gabor transform can thus be written as

$$\tilde{x}(\tau, \omega) = \int_{-\infty}^{\infty} x(t) g(t-\tau) e^{-i\omega t} dt, \tag{8}$$

where the Gaussian window function is given by

$$g(t-\tau) = A e^{-(t-\tau)^2/2a^2}. \tag{9}$$

Here, A can be used as a scaling factor and in practice is often set comparable to the amplitude of the signal of interest and there is no strict necessity for the scaling factor A. The parameter a, sets the window width as shown in Fig. 6. Although the limits in Eq. (8) extend to $\pm\infty$, in practice, the parameter a controls the width of the signal that is analyzed. We consider $4a$ to be the window length of the Gaussian window, because at this point $g(t-\tau)$ has decreased to e^{-2} on each side of the time τ. As $a \to \infty$, the conventional Fourier transform is recovered and there is no windowing or modification to the original time signal $x(t)$. As a decreases, the window becomes progressively narrower so that temporal localization improves.

For real discrete time signals such as the digitized strain or stress signals received from the A/D converter of a rheometer, a discrete Fourier transform of the product of the incoming time signal with the discretized Gaussian window is taken, as represented in Eq. (4) instead of a Fourier transform involving integrals.

B. Amplitude correction due to windowing

Although the Gabor transformation provides effective time localization, because of the summation present in Eq. (4), the window function reduces the amplitude of the Fourier-transformed variable $\tilde{x}(\tau, \omega)$. In rheometry, we need precise values of the amplitude in order to correctly compute quantities such as the dynamic modulus so this amplitude reduction needs to be systematically corrected. To illustrate this, we again consider a sinusoidal signal $x(t) = \sin(\omega_i t_n)$ with the number of discrete points fixed at $N = 2048$, a total

duration of the signal $T = 40\pi$ and $\omega_i = 1$ rad/s. A Gaussian window with $a = 20$ s located at $\tau = 20\pi$ s is considered. The windowed signal, which is the product of the time signal $x(t)$ and the Gaussian window $g(t - 20\pi)$, is shown in Fig. 7(a). The calculated amplitude spectrum from the discrete Fourier transform of the windowed signal is different from the amplitude spectra of the discrete time signal $x(t_n) = \sin(\omega_i t_n)$ evaluated without any windowing. This is shown by the difference between the blue dotted line which corresponds to the amplitude spectrum of the windowed signal and the red broken line which corresponds to the amplitude spectrum of the raw time signal $x(t_n) = \sin(\omega_i t_n)$ without any windowing in Fig. 7(b). Thus, in order to determine the correct value of the complex modulus from a discrete Gabor transform which includes windowing, we must use an amplitude correction factor A_w [63] given by

$$A_w = \frac{N}{\sum_{n=0}^{n=N-1} g(t_n)}, \tag{10}$$

where N is the total number of points in the discrete time signal, $t_n = n \cdot dt$ as defined in Sec. II A, and $g(t_n)$ is the value of the Gabor window function at time t_n. Using this correction factor, we can now write the relationship between the discrete Fourier transform and the discrete Gabor transform at the frequency of interest (ω_i) as

$$\tilde{x}_{\mathrm{DFT}}(\omega = \omega_i) = \tilde{x}_{\mathrm{STFT}}(\omega = \omega_i) \cdot A_w. \tag{11}$$

The black solid line in Fig. 7(b) shows the amplitude spectrum of the discrete Gabor transform after correction. The peak value now coincides with the peak value of the DFT of the original unwindowed time signal. By using this procedure, the discrete Gabor transform (or any other windowed STFT) can be easily employed to obtain the correct value of the complex moduli from the output stress or strain signal at the specified frequency of interest.

C. Estimation of optimal window length

Careful inspection of Fig. 7(b) shows that although Eq. (11) enabled us to correct the amplitude of the transformed signal, the windowing algorithm also has broadened the width of the peak. It remains to understand how the selection of the window length affects the spectral and temporal resolution of our Gabor transform, and if there is an optimal value of the parameter a. In order to find the relationship between the window length and frequency resolution of the time signal, a discretely sampled simple cosinusoidal signal $x_0\cos(\omega_i t_n)$ is considered. The discrete Fourier transform of the cosine signal at a specific angular frequency ω_i of interest yields (provided signal periodicity)

$$\tilde{x}_{\mathrm{DFT}}(\omega_k = \omega_i) = \sum_{n=0}^{N-1} x_0 \cos(\omega_i t_n) e^{-i\omega_i t_n} = x_0 N/2, \tag{12}$$

where N is the total number of points in the digital signal. The discrete Gabor transform (DGT) of $x = x_0\cos(\omega_i t_n)$ at ω_i is just the DFT of the time signal after multiplication with a Gaussian window

$$\tilde{x}_{\mathrm{DGT}}(\omega_i, t_k) = \sum_{n=0}^{N-1} x_0 \cos(\omega_i t_n) \frac{1}{\sqrt{2\pi}a} e^{-(t_n - t_k)^2/2a^2} e^{-i\omega_i t_n}. \tag{13}$$

Here, t_k (where $k = 0, 1, \ldots N-1$) is considered the arbitrary time of interest at which we seek to obtain temporal resolution [i.e., the equivalent of τ in the integral form in Eq. (8)]. In order to obtain the correct peak value at the frequency of interest ω_i at $t = t_k$, the amplitude correction factor A_w is multiplied with the discrete Gabor transform. Therefore, the rescaled form of Eq. (13) becomes

$$\tilde{x}_{\mathrm{DGT}}(\omega_i, t_k) = x_0 N \frac{\sum_{n=0}^{N-1} \cos(\omega_i t_n) e^{-(t_n - t_k)^2/2a^2} e^{-i\omega_i t_n}}{\sum_{n=0}^{N-1} e^{-(t_n - t_k)^2/2a^2}}. \tag{14}$$

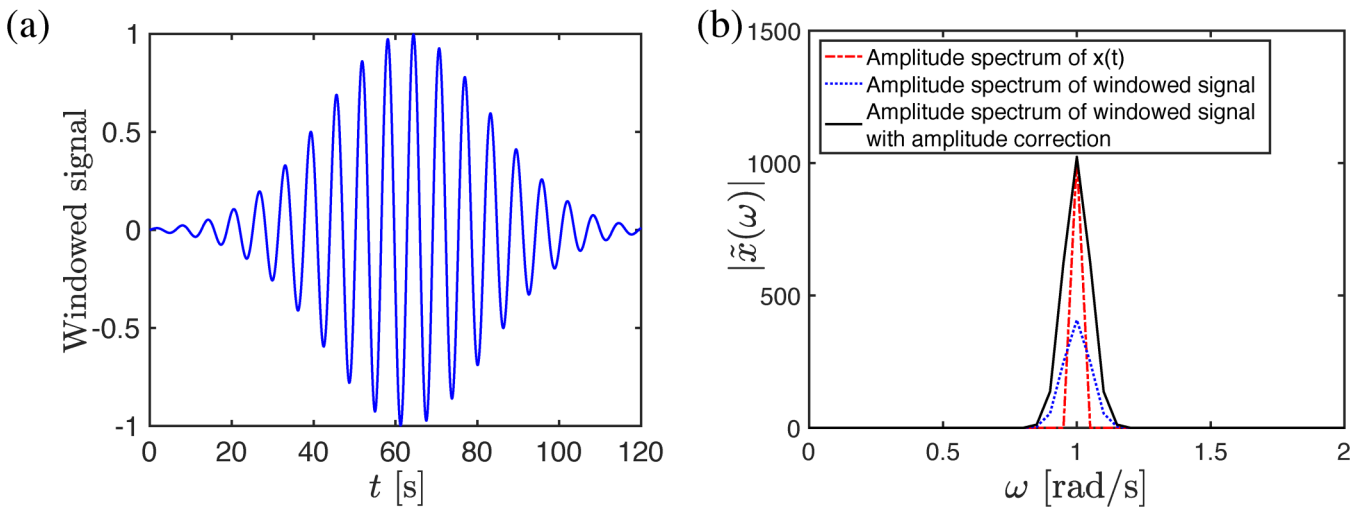

FIG. 7. The windowed signal shown is the product of $x(t)g(t - \tau)$ for a value of $\tau = 20\pi$ s, where $x(t) = \sin(\omega_i t)$ with $\omega_i = 1$ rad/s and $g(t - \tau)$ is the Gaussian function as given in Eq. (9). (b) The amplitude spectrum of the transformed signal $\tilde{x}(\omega)$ is shown by the red broken line. The amplitude spectrum of the windowed signal is represented using a blue dotted line and the amplitude spectrum of the windowed signal multiplied with the amplitude correction is shown as the black solid line.

Writing the cosine function in terms of $(e^{i\omega_i t_n} + e^{-i\omega_i t_n})/2$, Eq. (14) can be simplified to

$$\tilde{x}_{\mathrm{DGT}}(\omega_i, t_k) = \left(\frac{x_0 N}{2}\right)\left(\frac{\sum_{n=0}^{N-1} e^{-(t_n-t_k)^2/2a^2}(1+e^{-i2\omega_i t_n})}{\sum_{n=0}^{N-1} e^{-(t_n-t_k)^2/2a^2}}\right). \tag{15}$$

We further simplify Eq. (15) as

$$\frac{\tilde{x}_{\mathrm{DGT}}(\omega_i, t_k)}{\left(x_0 N/2\right)} = \left(1 + \frac{\sum_{n=0}^{N-1} e^{-(t_n-t_k)^2/2a^2} e^{-i2\omega_i t_n}}{\sum_{n=0}^{N-1} e^{-(t_n-t_k)^2/2a^2}}\right). \tag{16}$$

It is clear from Eq. (16) that in the limit $a \to \infty$, the expression for $\tilde{x}_{\mathrm{DGT}}$ approaches the discrete Fourier transform result ($\tilde{x}_{\mathrm{DFT}}$) we seek. However, in this limit we lose the temporal resolution. In order to accurately approximate the discrete Fourier transform through a discrete Gabor transform, we require the error in Eq. (16) to be small, i.e.,

$$\left|\frac{\sum_{n=0}^{N-1} e^{-(t_n-t_k)^2/2a^2} e^{-i2\omega_i t_n}}{\sum_{n=0}^{N-1} e^{-(t_n-t_k)^2/2a^2}}\right| \ll 1. \tag{17}$$

The expression above can also be expressed as

$$\left|\frac{\sum_{n=0}^{N-1} e^{-(t_n-t_k)^2/2a^2}(\cos(2\omega_i t_n) + i\sin(2\omega_i t_n))}{\sum_{n=0}^{N-1} e^{-(t_n-t_k)^2/2a^2}}\right| \ll 1. \tag{18}$$

The oscillatory nature of the harmonic functions in the numerator of Eq. (18) is important in considering the error in a discrete Gabor transform. After amplitude correction the error oscillates about the correct value (as obtained from DFT), with a frequency which is two times the frequency ω_i of the test signal. For large N, the error term in Eq. (18) can be approximated as

$$\approx \frac{\int_{-\infty}^{\infty} e^{-(t_n-t_k)^2/2a^2}(\cos(2\omega_i t_n) + i\sin(2\omega_i t_n))dt_n}{\int_{-\infty}^{\infty} e^{-(t_n-t_k)^2/2a^2} dt_n}. \tag{19}$$

Note that this approximation of a summation by an integral fails for t_k close to the edges of the experimental window due to the partial truncation of one side of the Gaussian window, which results in an incomplete convolution between the Gaussian window with the time-varying signal. For this reason, it is recommended to limit the analysis to the time-domain from $2a \le t_k \le T - 2a$, where a is the window length and T is the total duration of the experimental time window. The amplitude of this error can then be evaluated as

$$\left|\frac{\int_{-\infty}^{\infty} e^{-(t_n-t_k)^2/2a^2} e^{i2\omega_i t_n} dt_n}{\int_{-\infty}^{\infty} e^{-(t_n-t_k)^2/2a^2} dt_n}\right| = e^{-2a^2\omega_i^2}. \tag{20}$$

We set a tolerance limit of 10^{-6} for the magnitude of the error in the discrete Gabor transform,

$$e^{-2a^2\omega_i^2} \le 10^{-6}. \tag{21}$$

From here, we obtain an inequality between the window length and the frequency of the input time signal in order to neglect the oscillatory error present in the discrete Gabor transform and approximate the transformed result as the discrete Fourier transform of the frequency of interest,

$$a\omega_i \ge 2.63 \tag{22}$$

or equivalently

$$4a \ge 1.68\left(\frac{2\pi}{\omega_i}\right), \tag{23}$$

if we write the criterion in terms of the period of oscillation and the window width $4a$ shown in Fig. 6. However, increasing the window length to obtain accurate modulus information at a specific frequency results in decreasing time resolution. The relationship between the window length and time resolution is demonstrated in Fig. 8, which shows the amplitude spectra calculated from application of the discrete Gabor transform to the signal in Fig. 4 for $\omega_i = 1$ rad/s. As the window length decreases from $4a = 16.8(2\pi/\omega_i) = 105.6$ s to $4a = 1.68(2\pi/\omega_i) = 10.56$ s, the time resolution of the step change discontinuity at $\tau = 20\pi$ s gets better. However, when the window length is reduced even further and the inequality in Eq. (23) is not satisfied, we observe the growth of an oscillatory error with a frequency of $2\omega_i$ as expected from Eq. (18). Hence, to achieve good time resolution and frequency resolution we select

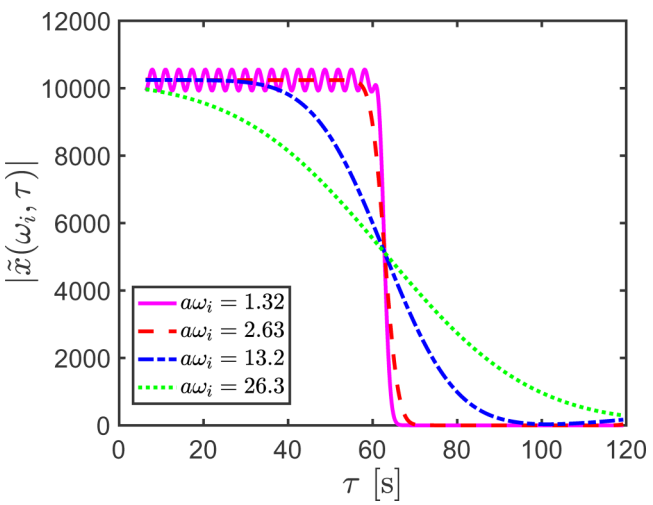

FIG. 8. Discrete Gabor transform at $\omega_i = 1$ rad/s of the time signal in Fig. 4 for different window lengths. The temporal resolution is improved as the window length shortens. However, when the window length becomes shorter than the constraint imposed by Eq. (24), i.e., $4a < 1.68(2\pi/\omega_i)$ (or $a\omega_i < 2.63$), where $\omega_i = 1$ rad/s is the frequency of the imposed sinusoid, then the oscillatory contribution to the error (which oscillates at a frequency $2\omega_i$) starts to dominate as shown by the magenta solid line with $a\omega_i = 1.32$.

$$4a = 1.68\left(\frac{2\pi}{\omega_i}\right) \tag{24}$$

to be the optimal window length (i.e., $a\omega_i = 2.63$). The Gabor transform technique can be viewed as a postprocessing analysis of the recorded time signal data. Therefore, in an experimental setting, it is feasible to run the experimental raw data through different values of the Gaussian window length "a" to obtain better time or better frequency resolution (high pass or low pass) according to the specific application. The same approach can be applied to the signal shown in Fig. 4 with a test frequency $\omega_i = 5$ rad/s. The results will again show improving time resolution as a is decreased. In general, for a multiwave input signal [48] which has multiple frequencies of interest, the value of ω_i in Eq. (24) should be the *lowest* frequency of interest so that the inequality expressed in Eq. (23) is satisfied for all frequencies present in the original time signal $x(t)$. The time-frequency uncertainty involved in extracting time and frequency information using the discrete Gabor transform and its dependence on window length is discussed in further detail in Appendix A.

It is also important to note that in order to provide temporal resolution, the Gaussian windowing effectively isolates a selected part of the whole time signal. This leads to a reduction of the effective number of points (N) for the Fourier transformation and a potential increase in spectral digitization noise. Thus digital over-sampling and box-car averaging of the digitized signal could be beneficial to retain accuracy in the time- and frequency-resolved material properties. A useful rule of thumb would be to oversample digitally on the A/D converter by a factor ($T/4a$) greater than the digital sampling used for a conventional discrete Fourier transform routine; where T is the time period of the signal and a is the window length.

IV. APPLICATIONS OF THE GABOR TRANSFORM

A. Extracting time-dependent complex moduli

In Subsections IIIA–IIIC, the discrete Gabor transform was introduced to overcome the limitations of the discrete Fourier transform, specifically the lack of temporal resolution and the assumption of time translation invariance. Data processing techniques for amplitude correction and identifying the optimal window length were discussed to enable use of the DGT to obtain accurate time- and frequency-resolved data. The resulting algorithm can be used for extracting time-dependent complex moduli data for a wide range of thixotropic and aging viscoelastic materials [45]. For such mutating materials, the time- and frequency-dependent complex modulus can be generally defined as

$$G^*(\omega, \tau) = \frac{\tilde{\sigma}_{\mathrm{STFT}}(\omega, \tau)}{\tilde{\gamma}_{\mathrm{STFT}}(\omega, \tau)}, \tag{25}$$

where $\tilde{\sigma}_{\mathrm{STFT}}$ is the STFT of the stress signal and $\tilde{\gamma}_{\mathrm{STFT}}$ is the STFT of the input strain signal.

To demonstrate the application of this idea, we first consider an aging Kelvin–Voigt model [47] to illustrate the capability of the discrete Gabor transform for extracting time-dependent moduli. The aging Kelvin–Voigt model, with a time-varying modulus and a constant viscosity, has been used by Coussot [47] for modeling the aging behavior of Bentonite clay, and the constitutive response can be written in the form

$$\sigma(t) = E(t)\gamma(t) + \eta_0\dot{\gamma}(t). \tag{26}$$

For the purpose of demonstration, we set the viscosity $\eta_0 = 2$ Pa s and set the modulus to be a linearly growing function of time

$$E(t) = 10 + 0.5t. \tag{27}$$

The storage modulus and the loss modulus for this time-varying Kelvin-Voigt model can be expressed analytically as:

$$G'(\omega, t) = E(t) = 10 + 0.5t, \tag{28}$$

$$G''(\omega, t) = \eta_0\omega. \tag{29}$$

An oscillatory strain signal of the form $\gamma(t) = \gamma_0\sin(\omega_i t)$ with $\gamma_0 = 0.1$ and $\omega_i = 10$ rad/s is used as the input to the aging Kelvin–Voigt model. The output stress is calculated from Eq. (26) and is plotted in Fig. 9(a). The amplitude of the stress signal increases linearly with time since the modulus increases linearly with time. The phase of the signal (relative to the input strain) also shifts with time due to the decreasing phase angle $\delta(t) = \tan^{-1}(\eta_0\omega/E(t))$, but this is difficult to discern from a representation such as Fig. 9. To extract the time-dependent complex moduli from the output stress signal and the input strain signal using the discrete Gabor transform, a Gaussian window of window length $4a = 1.68(2\pi/\omega_i) = 1.056$ s is translated along the output signal as shown schematically by the red Gaussian line in Fig. 9(a). The Gaussian window traverses the output stress signal and, as it travels across the signal, the windowed stress i.e., the product of the stress $\sigma(t)$ and the Gaussian window $g(t - \tau)$ at every discrete time instant is calculated. The windowed stress is shown in Fig. 9(b) at time $\tau = 32$ s and illustrates the time localization that is obtained. The time-resolved discrete Gabor transform, corresponding to the discrete Fourier transform of this windowed signal at every discrete time instant in the range $2a \leq t \leq T - 2a$ is calculated (where T is the time duration of the stress and strain signal). This process is also followed for the input strain signal as well, and using Eq. (25), the time-resolved value of the complex modulus is obtained (however, a conventional Fourier transform could also be used here for the strain since the signal is stationary in time.). The real and imaginary components are shown in Fig. 9(c). The storage modulus (red data points) and the loss modulus (blue data points) calculated using the discrete Gabor transform (up to the illustrated point $\tau = 32$ s) are in excellent agreement with the analytical solutions for the storage and loss modulus represented by the red and blue solid lines respectively in Fig. 9(c). A similar analysis for an aging Kelvin–Voigt model is performed in Appendix B using piece-wise rectangular windows as well as Gaussian windows of different window lengths. This additional analysis shows that the Gaussian window performs better (in the sense of

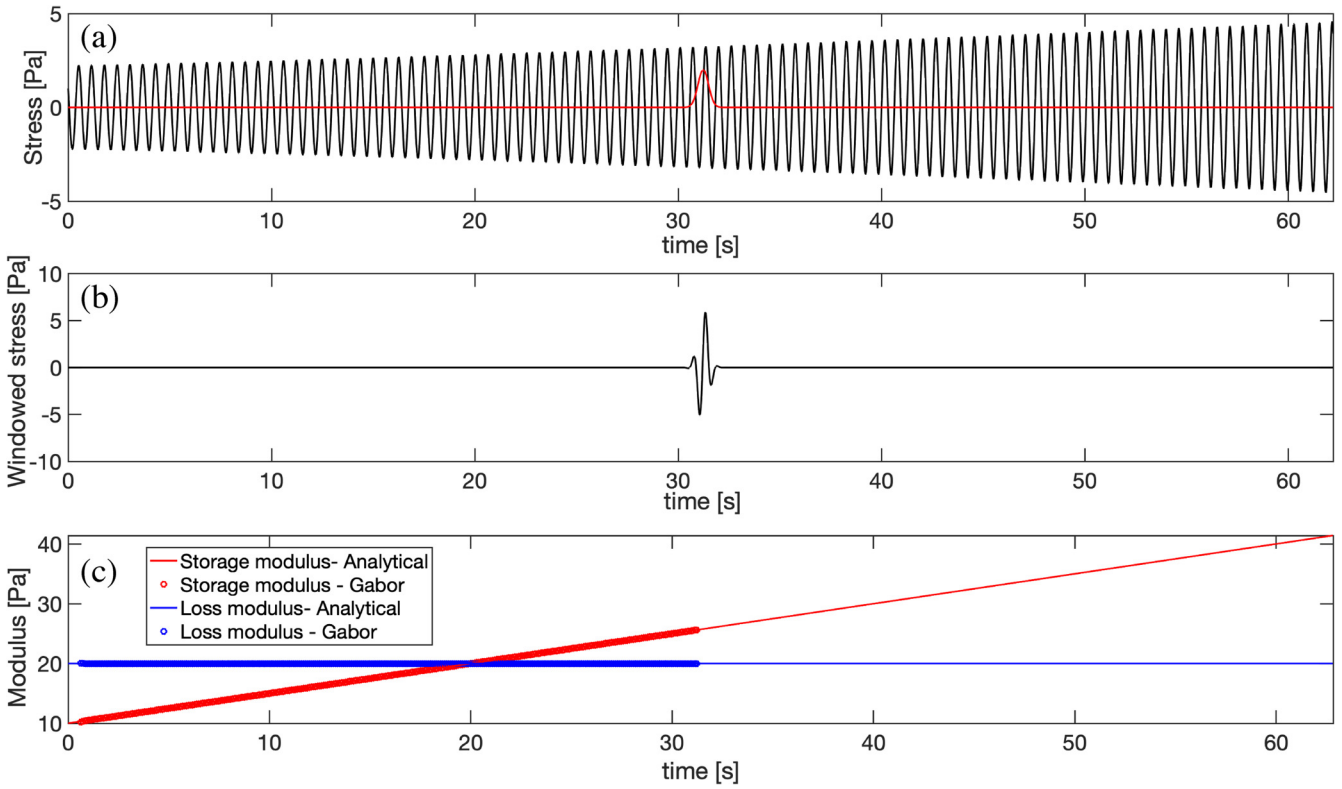

FIG. 9. (a) The output stress from the aging Kelvin–Voigt model given by Eqs. (26) and (27) for an input of $\gamma(t) = \gamma_0 \sin(\omega_i t)$ where $\gamma_0 = 0.1$ and $\omega_i = 10$ rad/s is illustrated by the black solid line. The Gaussian window with $4a = 1.68(2\pi/\omega_i) = 1.056$ s window, which traverses across the output signal is represented by the red solid line at $\tau = 32$ s. (b) The windowed output signal in time at $\tau = 32$ s. (c) The time-dependent evolution of the complex moduli for $\omega_i = 10$ rad/s. The red solid line and the red data points show, respectively, the analytical solution Eq. (28) and data obtained from the DGT for the storage modulus. Similarly, the blue solid line and the blue data points represent, respectively, the analytical solution of Eq. (29) and the data for the loss modulus obtained from the DGT. Please find a video illustrating implementation of the Gabor transform here. Multimedia view: https://doi.org/10.1122/8.0000549.1.

greater accuracy) than a piece-wise rectangular window. The analysis presented in Appendix B also helps in determining the window length for optimal time-frequency resolution [i.e., for giving minimum error in extracting $G'(\omega_i, t)$ and $G''(\omega_i, t)$]. The theoretical window length suggested by Eq. (24) is in excellent agreement with the optimal window length results determined numerically in Appendix B.

We now consider application of the DGT to experimental data obtained in SAOS using a 5 wt. % bentonite dispersion, a soft glassy material [32]. The material is first pre-sheared at 500 s^{-1} for 30 s to eliminate residual microstructure. We then apply an oscillatory stress input of $\sigma = \sigma_0 \sin(\omega_i t)$ where $\sigma_0 = 0.1$ Pa and $\omega_i = 1$ rad/s. We run this experiment for a time duration of 300 s. The digitized signal from typical rheometric hardware can be noisy and therefore, we recommend oversampling for real world experiments as outlined in [52,64]. The time-evolving Lissajous curve of the measured strain $\gamma(t)$ vs input stress $\sigma(t)$ is shown in Fig. 10(a). The shape and orientation of the Lissajous orbits evolve with time as the modulus of the aging fluid increases. Following the same procedures described for extracting the time-dependent complex modulus for the aging Kelvin–Voigt model above, we can use the DGT ($a\omega_i = 2.63$) to obtain the time-resolved complex moduli of this bentonite dispersion. The storage modulus (red data points) increases steadily with aging time as seen in the model calculation presented in Fig. 10(b). This demonstrates the physical aging behavior of this soft glassy material. A logarithmic fit to the measured data gives a characteristic thixotropic time scale for this bentonite dispersion of $\tau_{thix} \cong 8.43$ s. The DGT also shows that there is no dependence of the loss modulus on age time for this bentonite dispersion, indicating that the material becomes more elastic or gel-like with time, but the viscous contribution to the linear viscoelastic response remains invariant with time.

B. Extracting dynamic modulus and compliance from transient startup of oscillatory flow

Observing a complex transient response during the start up of oscillatory shear flow is common in stress-controlled rheometers. The secular terms (i.e., the decaying transient and the final DC offset from the initial zero mean strain) are dominant at the inception of the oscillatory flow and must be removed before analysis of the final alternance state. Hence, the conventional procedure for measuring the steady state compliance $J'(\omega)$ and $J''(\omega)$ is to wait for the transient response to decay before data collection is started. It has been recently suggested [65] that understanding this initial transient response would allow more rapid determination of the viscoelastic response of complex fluids. Here, we demonstrate the use of discrete Gabor transforms to obtain accurate material property information from the initial transient data as well as steady state data simultaneously. To illustrate the approach, we consider a two-mode generalized Maxwell model consisting of two series arrangements of a spring and a dashpot that are

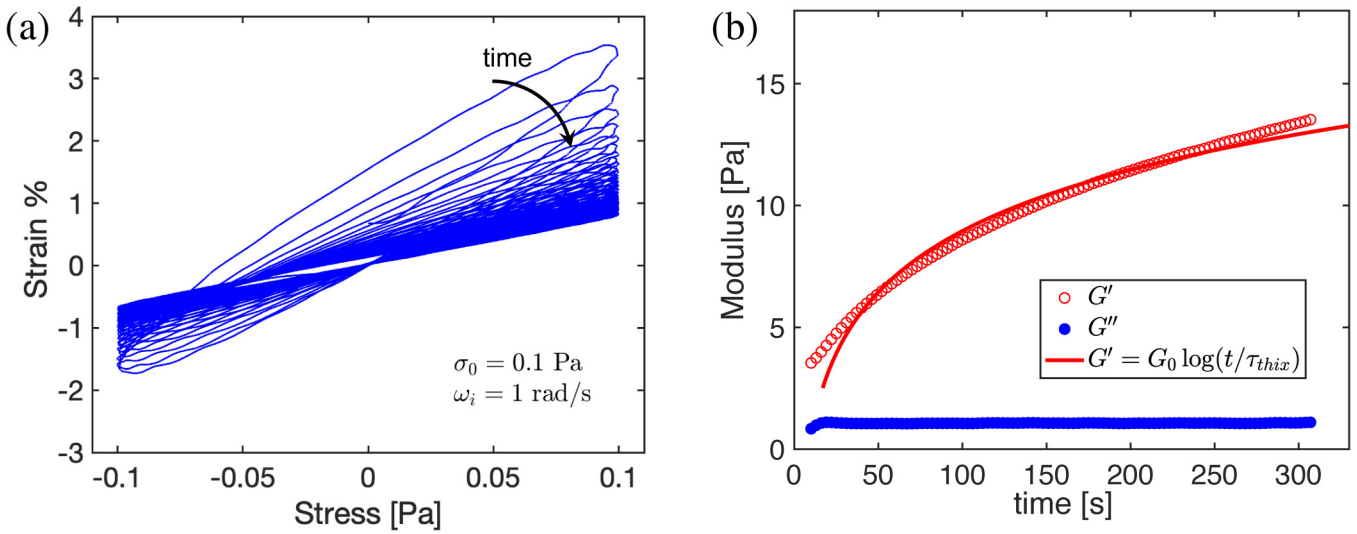

FIG. 10. (a) Time-evolving Lissajous curves for a small amplitude oscillatory stress (SAOStress) test with a 5 wt. % bentonite dispersion for an input waveform of $\sigma(t) = \sigma_0 \sin(\omega_i t)$ where $\omega_i = 1$ rad/s and $\sigma_0 = 0.1$ Pa. (b) The time-resolved components of the complex modulus for $\omega_i = 1$ rad/s are shown. The red data points and the blue data points represent the storage and loss modulus data obtained from the DGT respectively. The red solid line represents a logarithmic aging fit: $G'(t) = G_0 \log(t/\tau_{thix})$, where $G_0 = 3.62$ Pa and $\tau_{thix} = 8.43$ s is the thixotropic time scale for the fluid.

aligned in parallel to each other. An analytical solution for the damped oscillatory response following inception of an oscillatory stress are derived in [66]. The input to the system is given generically by $\sigma = \sigma_0 \sin(\omega t + \psi)$ where ψ is a phase lag, $0 < \psi < \pi/2$. The resulting output strain from the system is composed of three terms

$$\gamma(t) = \sigma_0 \Big(J'(\omega)\sin(\omega t + \psi) - J''(\omega)\cos(\omega t + \psi) \Big) + \sigma_0 \frac{\cos(\psi)}{\omega(\eta_1 + \eta_2)} + \gamma_t(t), \tag{30}$$

where the first term in parentheses represents the alternance (steady state) response (with J' and J'' the dynamic storage and loss compliance respectively), the second term represents the nonzero offset to the strain (which depends on the selected phase angle ψ) and the last term represents the secular or transient term. Hassager [66] uses Laplace transforms to show that this last term can be written analytically as

$$\gamma_t = \sigma_0 \frac{(\omega\lambda\cos(\psi) - \sin(\psi))\eta_1\eta_2(\tau_1 - \tau_2)^2}{(1 + (\lambda\omega)^2)(\eta_1 + \eta_2)^2(\tau_1\eta_2 + \tau_2\eta_1)} e^{-t/\lambda}, \tag{31}$$

where η_1, τ_1 and η_2, τ_2 are the viscosity and relaxation time of each Maxwell mode, respectively, and the single retardation time for the two mode Maxwell mode is

$$\lambda = \frac{\eta_1\tau_2 + \eta_2\tau_1}{\eta_1 + \eta_2}. \tag{32}$$

The model parameters for our illustrative example are chosen as follows: $\sigma_0 = 1$ Pa, $\eta_1 = 1$ Pa s, $\eta_2 = 10$ Pa s, $\tau_1 = 10$ s, $\tau_2 = 0.01$ s, $\omega = 52$ rad/s, and $\psi = 0$. The retardation time is thus $\lambda = 9.09$ s. The initial oscillatory response of the system is shown in Fig. 11(a).

To evaluate the steady state and the transient terms, the Gaussian window with $a\omega_i = 3.5$ [a wider window than Eq. (24) to account for the transient] is translated along the time signal and the discrete Gabor transform is calculated for $2a \le \tau \le T - 2a$ s for $T = 1.8$ s. The contribution to the secular term at each value of time probed corresponds to the instantaneous DC ($\omega = 0$) component in the discrete Gabor transform, and the complex compliance $J^*(\omega)$ is given by the real and imaginary components of the discrete Gabor transform at the frequency ($\omega_i = 52$ rad/s) of the input signal. The evolution with time of both the secular and the steady-state time periodic terms at ω_i are shown in Figs. 11(b) and 11(c), respectively. Clearly, both the transient and final periodic steady state components of the analytic solution are closely approximated. To quantify this, the error in our determination of the steady state compliance using the DFT can be defined as

$$\epsilon = \left| \frac{|J^*|_{DFT} - |J^*_{analytical}|}{|J^*_{analytical}|} \right|. \tag{33}$$

We investigate how this error varies for four different window lengths $a = 2.63{*}m/\omega_i$ (with $m = 1, 1.5, 2, 3$ and for a fixed value of $\omega_i = 52$ rad/s) and compute the error ϵ using the parameter values given above. The resulting error is shown in Fig. 11(d) as a function of the number of cycles (n) of the output strain signal, which are considered for the calculation of the steady state complex compliance. It can be observed from Fig. 11(d) that the error incurred by the discrete Gabor transform decreases more rapidly than the error from the discrete Fourier transform. The asymptotic plateau value of the error (resulting from the discrete nature of the DGT and DFT) also decreases as the window length is increased. There is more flexibility for selecting the window length $a\omega_i$ in this application since there is no time dependence in the complex compliance $J^*(\omega)$. The trade-off is instead in terms of the time taken to measure the property vs the accuracy desired.

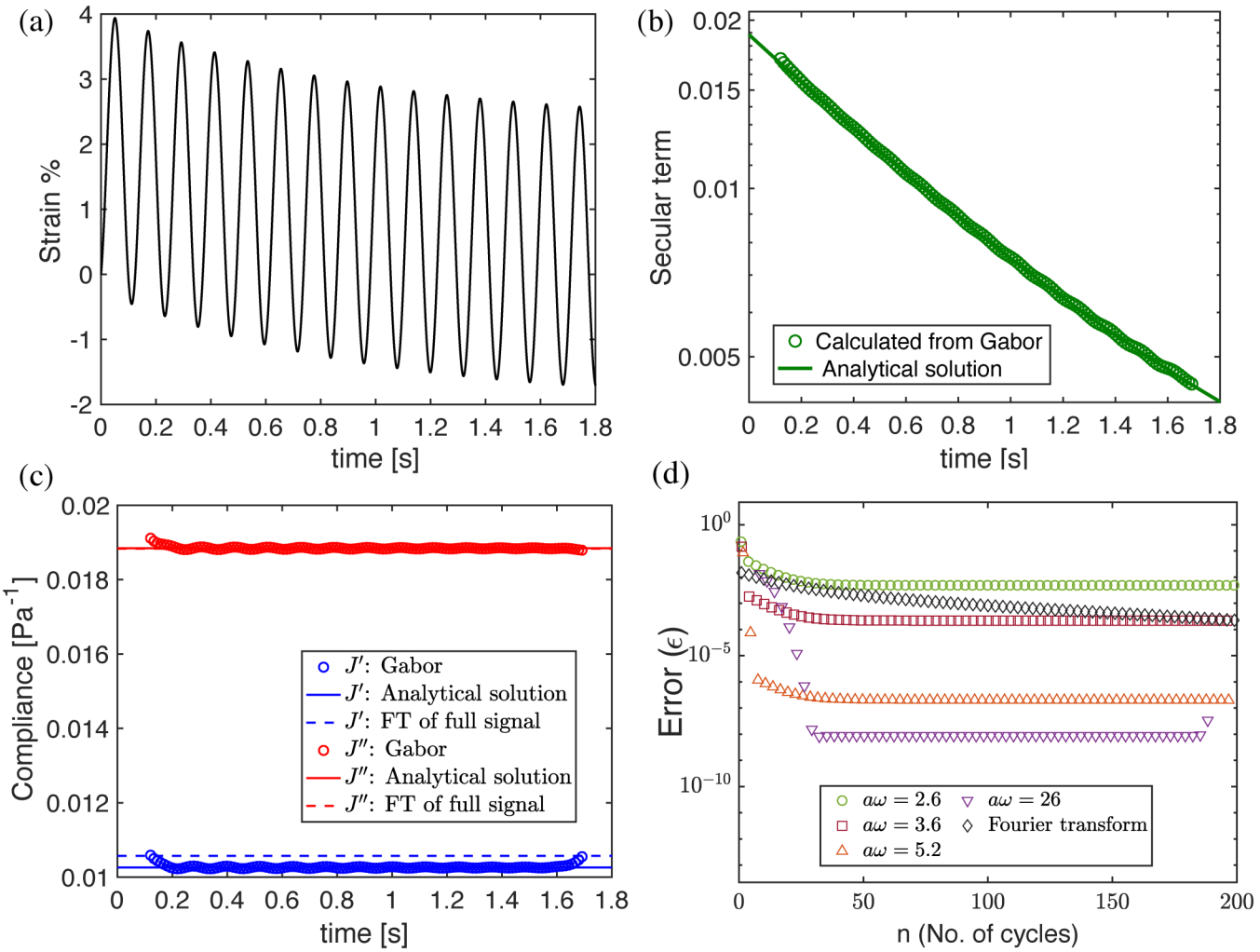

FIG. 11. (a) The transient response of a two-mode Maxwell model following inception of small amplitude oscillatory shearing. (a) The black solid line represents the output strain following initiation of small amplitude oscillatory stress at $t = 0$ with $\psi = 0$. (b) The evolving secular terms in the response are captured by the DC term of the Gabor transform spectrum. (c) The red and blue data points show time-resolved estimates of the elastic and viscous compliance obtained, respectively, from the DGT. The red and blue dashed lines represent the elastic and viscous compliance calculated from a DFT considering the entire time signal shown in (a). The red and blue solid lines represent the analytical solution for the elastic and viscous compliance, respectively, for the two-mode Maxwell model given by Eq. (30) with the specified parameters. (d) Mean square error given in Eq. (B3) as the number of cycles considered for the compliance calculation increases. Please find a video of this implementation of the Gabor transform here. Multimedia view: https://doi.org/10.1122/8.0000549.2.

C. Rapid extraction of nonlinear Fourier–Tschebyhev coefficients

Another potential application of Gaborheometry is in the rapid construction of a Pipkin diagram for a complex fluid. In the linear viscoelastic regime, data across different frequencies can be rapidly obtained using the OWCh protocol [49,51]. However, in the nonlinear regime, the material functions for a complex fluid are functions of both the frequency and amplitude of the oscillatory deformation. Conventional techniques that have been extensively used to probe the Pipkin diagram in this regime include MAOS and LAOS. In these methods a sinusoidal signal with a user-specified amplitude and frequency is selected as the input strain signal [16]

$$\gamma(t) = \gamma_0 \sin(\omega t). \tag{34}$$

This corresponds to a single coordinate point ω, γ_0 in the Pipkin diagram represented schematically in Fig. 12. The output stress in the nonlinear regime can then be written in terms of a Fourier series expansion

$$\sigma(t) = \gamma_0 \sum_{n:odd} G_n'\{(\omega, \gamma_0)\sin(n\omega t) + G_n''(\omega, \gamma_0)\cos(n\omega t)\}, \tag{35}$$

where $G_n'(\omega, \gamma_0)$ and $G_n''(\omega, \gamma_0)$ are the elastic and viscous nonlinear Fourier coefficients, respectively. When $\gamma_0 \to 0$, (i.e., in the linear regime), we expect $G_1'(\omega, \gamma_0) = G'(\omega)$ and $G_1''(\omega, \gamma_0) = G''(\omega)$. The output stress can also be decomposed in terms of Tschebyshev polynomials of the scaled strain and strain rate [8,11–13],

$$\sigma(t) = \gamma_0 \sum_{n:odd} e_n(\omega, \gamma_0)T_n(x) + \dot{\gamma}_0 \sum_{n:odd} v_n(\omega, \gamma_0)T_n(y), \tag{36}$$

where T_n is the nth order Tschebyshev coefficient of $x = \gamma/\gamma_0$ and $y = \dot{\gamma}/\dot{\gamma}_0$. The e_n coefficients are referred to as the elastic Tschebyshev coefficients and the v_n values are the viscous Tschebyshev coefficients [11]. The relationships between the viscoelastic moduli in the Fourier expansion and the elastic and viscous Tschebyshev coefficients are given by

$$e_n = G'_n(-1)^{(n-1)/2}, \tag{37}$$

$$v_n = G''_n/\omega. \tag{38}$$

These nonlinear Fourier and Tschebyshev coefficients can be determined for different input strain amplitudes and frequencies as indicated schematically by the green data points in Fig. 12. Therefore, for a particular oscillatory frequency of deformation, in order to find the dependence of $G'_n(\omega, \gamma_0)$ or $G''_n(\omega, \gamma_0)$ on strain amplitude or just to plot the evolution of these nonlinear Fourier coefficients with γ_0, one requires many LAOS experiments at a sequence of successively larger strain amplitudes. Probing the entire Pipkin diagram can, therefore, be time consuming [17,22].

We thus, consider using an amplitude-modulated input signal to perform a slow amplitude sweep at a specified deformation frequency and then using Gaborheometry to extract the instantaneous strain-evolving Fourier coefficients as a function of input amplitude from a single experiment. This protocol is represented schematically by the vertically oriented oscillatory solid line shown in Fig. 12. This AM signal processing technique reduces the number of experiments required to probe the Pipkin diagram as well as post-processing time. Using Gaborheometry, we can obtain the dependence of the nonlinear Fourier–Tschebyshev coefficients on input strain amplitude for a specified deformation frequency from a single experiment; i.e., we can compute values of $G'_n(\omega, \gamma_0)$ or $G''_n(\omega, \gamma_0)$, or equivalently e_n and v_n, for a specified frequency using a discrete Gabor transform at each instantaneous value of the strain $\gamma_0(t)$.

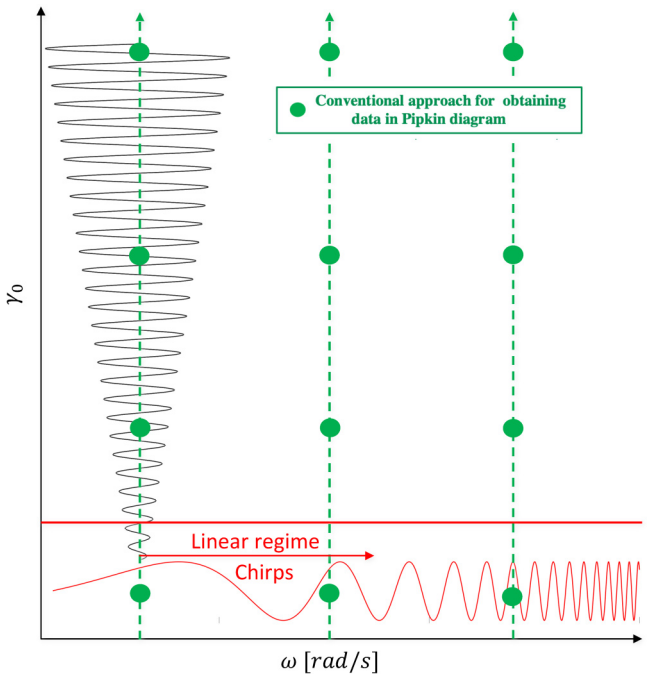

FIG. 12. General representation of the Pipkin space for a complex fluid in terms of frequency ω and input strain amplitude γ_0. Chirps serve as a quick way to obtain the linear frequency response of a material. The conventional way of obtaining nonlinear Fourier–Tschebyshev coefficients by specifying a single input pair γ_0, ω (indicated by each green point) and then imposing a strain input of the form given in Eq. (34) can be time consuming. A more rapid method of obtaining nonlinear Fourier–Tschebyshev coefficients for a specified deformation frequency using amplitude-modulated (AM) ramps to construct the Pipkin diagram is illustrated.

To demonstrate this technique, we consider a linearly increasing amplitude-modulated input strain signal with ramp rate r, so the instantaneous value of the strain is

$$\gamma(t) \equiv \gamma_0(t)\sin(\omega t) = \gamma_i(1 + rt/\gamma_i)\sin(\omega t), \tag{39}$$

where γ_i is the initial amplitude of the modulated signal. The Gaussian window $g(t - \tau)$, which is then passed over the time signal calculates the windowed signal over a window length set by the chosen value of a and guided by the discussion in Sec. III C. Of course now we have the additional constraint that, within a single oscillatory cycle, the input strain amplitude should not change significantly so that we can approximate the oscillatory windowed output signal as a result of an approximately constant input amplitude. Therefore, to obtain a relevant constraint, at any time instant t we require

$$\frac{\gamma_0(t + 2\pi/\omega) - \gamma_0(t)}{\gamma_0(t)} \ll 1 \tag{40}$$

or equivalently, using Eq. (39), we can write

$$\frac{2\pi}{\omega}\frac{r}{\gamma_i + rt} \ll 1. \tag{41}$$

This dimensionless ratio controls the rate of change of the driving signal and may be considered a dimensionless ramp rate. The Gaborheometry examples considered in Secs. IV A and IV B correspond to $r = 0$. For an amplitude-modulated experiment this ramp rate is nonzero. We may set a tolerance limit and expect that the nonlinear coefficients determined for a given strain amplitude $\gamma_i + rt$ at a particular time t are accurate when the mutation number of the input signal

$$Mu_{amp} = \frac{2\pi}{\omega}\frac{r}{\gamma_i + rt} \ll 1. \tag{42}$$

Our computational tests show that typically we require $Mu_{amp} < 0.1$. To demonstrate this technique for obtaining the nonlinear Fourier or Tschebyshev coefficients from a single experiment, we consider the K-BKZ time-strain separable (TSS) constitutive model [18,23,67,68]

$$\sigma(t) = \int_{-\infty}^{t} M(t - t')h(\gamma(t, t'))\gamma(t, t')dt', \tag{43}$$

where $M(t - t')$ is the memory function of the material and

$h(\gamma)$ is a strain damping function which captures the nonlinearity observed when the imposed strain amplitude increases. Here, we consider a simple asymptotic expansion for $h(\gamma) \cong 1 + A\gamma^2 + O(\gamma^4)$, where A is the leading order damping coefficient and is typically negative for strain-softening materials. For example, the corotational Maxwell model corresponds to $A = -1/6$ [18]. For the purpose of demonstration, we consider the memory function to simply follow a single mode Maxwell response,

$$M(t - t') = \frac{\eta}{\lambda^2} e^{-(t-t')/\lambda}, \tag{44}$$

where η is the zero shear viscosity and λ is the relaxation constant of the model material. The numerical values for all the parameters used in this K-BKZ-TSS simulation are $\eta = 1$ Pa s, $\lambda = 2$ s, and $A = -0.6$. The amplitude-modulated input signal considered here is

$$\gamma(t) = (\gamma_i + rt)\sin(\omega t). \tag{45}$$

We consider an initial strain amplitude of 1% or $\gamma_i = 0.01$, ramp rate $r = 0.003\ \mathrm{s}^{-1}$, total time $t_f = 226$ s, and the specified frequency of deformation is $\omega = 1$ rad/s. The input strain given by Eq. (45) is substituted in Eq. (43) with the specified memory function and the damping function to evaluate the output stress. The resulting continuously varying Lissajous curve representing the response between the output stress and the input amplitude-modulated strain for the K-BKZ-TSS model with the specified parameters is shown in Fig. 13. As, we note above, this curve is all that is needed to calculate the evolution in the Fourier-Tschebyshev coefficients with strain amplitude.

The corresponding output stress is shown as a time series in Fig. 14(a). The Gaussian window $g(t - \tau)$ with $a\omega = 2.63$ is passed along the time signal and the windowed signal at every time instant $t - \tau = 0$ corresponds to an input strain signal of amplitude $\gamma_i + r\tau$. The real and imaginary part of the nth harmonic component of the discrete Gabor transform at time $t = \tau$ corresponds to $G'_n(\omega, \gamma_i + r\tau)$ and $G''_n(\omega, \gamma_i + r\tau)$, respectively. These Fourier coeffecients can also be interconverted to the corresponding elastic and viscous Tschebyshev coefficients using Eqs. (37) and (38), respectively. The values of G'_1, G'_3 and G''_1, G''_3 computed from the discrete Gabor transform are plotted as red and blue curves, respectively in Figs. 14(c)–14(f). The analytical solution for Fourier-Tschebyshev coefficients for the K-BKZ-TSS model with a Maxwell kernel and a damping function of the form $h(\gamma) = 1 + A\gamma^2$ have been derived by Martinetti and Ewoldt [18],

$$\frac{G'_1(\omega, \gamma_0)}{G_0} = \frac{e_1(\omega, \gamma_0)}{G_0} = \frac{\mathrm{De}^2}{1 + \mathrm{De}^2} + A\gamma_0^2 \frac{9\mathrm{De}^4}{(1 + \mathrm{De}^2)(1 + 4\mathrm{De}^2)}, \tag{46}$$

$$\frac{G''_1(\omega, \gamma_0)}{G_0} = \frac{v_1(\omega, \gamma_0)}{G_0/\omega} = \frac{\mathrm{De}}{1 + \mathrm{De}^2} + A\gamma_0^2 \frac{(9/2)\mathrm{De}^3}{(1 + \mathrm{De}^2)(1 + 4\mathrm{De}^2)}, \tag{47}$$

$$-\frac{G'_3(\omega, \gamma_0)}{G_0} = \frac{e_3(\omega, \gamma_0)}{G_0} = A\gamma_0^2 \frac{9\mathrm{De}^4(\mathrm{De}^2 - 1)}{(1 + \mathrm{De}^2)(1 + 4\mathrm{De}^2)(1 + 9\mathrm{De}^2)}, \tag{48}$$

$$\frac{G''_3(\omega, \gamma_0)}{G_0} = \frac{v_3(\omega, \gamma_0)}{G_0/\omega} = A\gamma_0^2 \frac{(3/2)\mathrm{De}^3(1 - 11\mathrm{De}^2)}{(1 + \mathrm{De}^2)(1 + 4\mathrm{De}^2)(1 + 9\mathrm{De}^2)}, \tag{49}$$

where $\mathrm{De} = \lambda\omega$ and $G_0 = \eta/\lambda$. The analytical solutions for the first four Fourier coefficients are plotted using red and blue solid lines in Figs. 14(c)–14(f). It is clear that the data points obtained using the discrete Gabor transform of the time series at each value of τ corresponding to an instantaneous strain $\gamma_0 = \gamma_i + r\tau$ are in good agreement with the analytical solution for the nonlinear Fourier–Tschebyshev coefficients. Close inspection of Figs. 14(c) and 14(d) shows that there is a small but systematic deviation at early times. This initially may seem puzzling since the input strain amplitude is smallest here; however, it can readily be explained by considering the temporal evolution of the mutation number Mu_{amp} defined in Eq. (42). Because γ_i chosen in this example is so small (0.01), the dimensionless ramp rate is initially large even though $r = 0.003\ \mathrm{s}^{-1}$. When the dimensionless ramp rate or mutation number plotted in Fig. 14(b) decreases to less than 0.1 the errors in the values of the coefficients obtained from the DGT become negligible. This serves to illustrate that it is important to choose the initial imposed strain and ramp rate of amplitude modulation carefully in

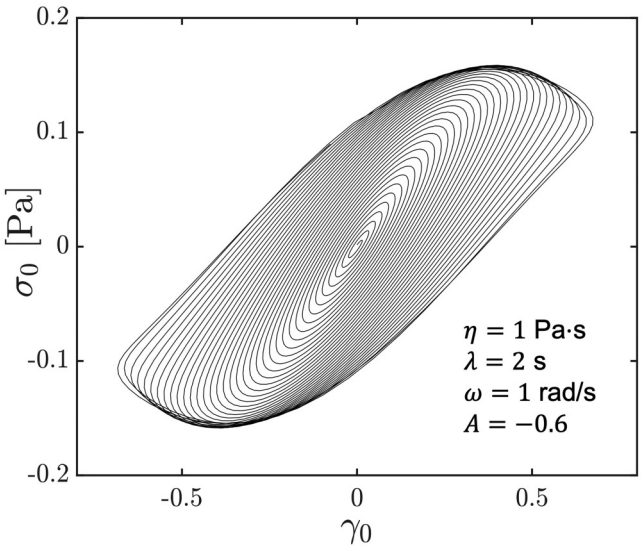

FIG. 13. The Lissajous curve for an amplitude-modulated input strain given by $\gamma = (\gamma_i + rt)\sin(\omega t)$ where $\gamma_i = 0.01$, $r = 0.003\ \mathrm{s}^{-1}$, and $\omega = 1$ rad/s to a K-BKZ-TSS constitutive equation with a relaxation modulus described by a single mode Maxwell model characterized by parameters η and λ in the memory function and a simple quadratic damping function $h(\gamma) = 1 + A\gamma^2$ as the damping function.

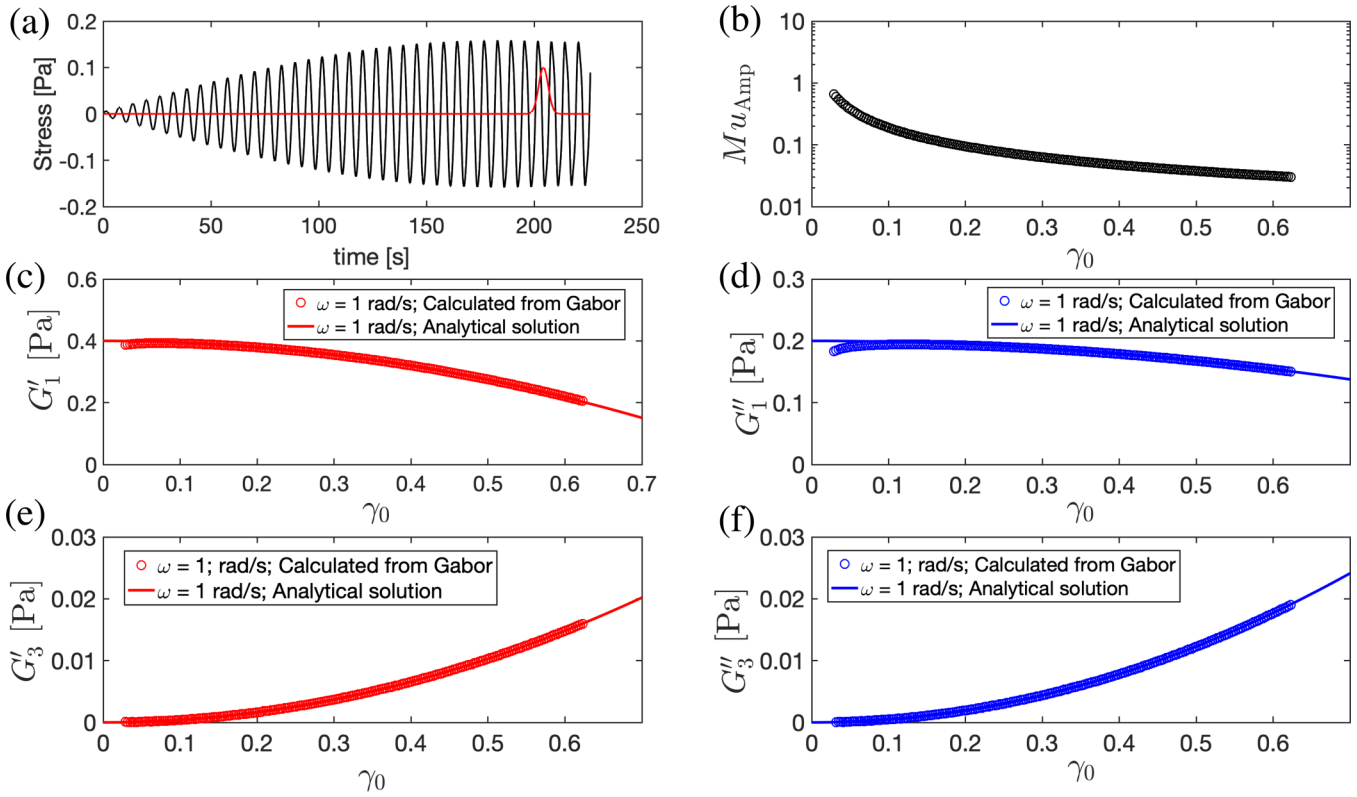

FIG. 14. Amplitude modulated Gaborheometry. (a) Output stress represented by the black solid line is from amplitude-modulated strain input, $\gamma(t) = (\gamma_i + rt)\sin(\omega t)$, where $\gamma_i = 0.01$, $r = 0.003\ \mathrm{s}^{-1}$, and $\omega = 1$ rad/s, which is supplied as input to a K-BKZ-TSS constitutive equation with a single mode Maxwell model (with parameters η and λ) as a memory function and $h(\gamma) = 1 + A\gamma^2$ as the damping function. Here, $\eta = 1$ Pa s, $\lambda = 2$ s, $A = -0.6$. The red solid line indicates the Gaussian window at specific instant $\tau = 205$ s which traverses across different stress amplitudes. (b) Evolution of the mutation number given by Eq. (41) with time or strain amplitude $\gamma(t)$. (c) Evolution in the first elastic Fourier coefficient $G_1'(\gamma_0)$. (d) Evolution in the first viscous Fourier coefficient G_1''. (e) Evolution in the nonlinear third harmonic elastic coefficient G_3'. (f) Evolution in the nonlinear third harmonic viscous coefficient G_3''. The data points are obtained from DGT and the solid lines represent the analytical solution. Please find a video of implementation of Gabor transform here. Multimedia view: https://doi.org/10.1122/8.0000549.3.

order to obtain accurate values of both the linear and the nonlinear Fourier or Tschebyshev coefficients using our Gabor transform technique from a single amplitude-modulated ramp.

D. Amplitude-modulated ramps for weakly mutating materials

Finally, we discuss here the potential of extending this amplitude-modulated protocol for time-evolving or mutating materials as well. There are now two time scales and two dimensionless mutation numbers to consider; one characterizing the rate of change of the imposed strain amplitude, and another characterizing the rate of change in the material itself. To explore this additional complexity in a systematic manner, we first consider here a suitable "toy model" composed of a mutating nonlinear constitutive response of the Kelvin–Voigt form [8]

$$\sigma(t) = f(\gamma, t)\gamma + g(\dot{\gamma})\dot{\gamma}, \tag{50}$$

$$f(\gamma, t) = G_0 + G_\beta(t)\left(\frac{\gamma}{\gamma^*}\right)^2, \tag{51}$$

$$g(\dot{\gamma}) = \eta_0 - \eta_\beta\left(\frac{\dot{\gamma}}{\dot{\gamma}^*}\right)^2, \tag{52}$$

Here, $f(\gamma, t)$ is the nonlinear elastic modulus that is also aging (or evolving with time) according to Eq. (51) and γ^* is the critical strain beyond which nonlinear elastic effects become significant. Similarly, $g(\dot{\gamma})$ is the nonlinear viscosity function and $\dot{\gamma}^*$ is the critical strain rate beyond which nonlinear viscous effects become significant. In order to introduce time-dependence or rheological aging, we make the coefficient G_β in Eq. (51) a function of time with a simple linear form $G_\beta = c_0 + t/\tau_{thix}$. We could also readily consider a logarithmic aging function (motivated by our experiments with the bentonite clay [Figs. 9 and 10]) but here we seek the simplest possible functional form. With these assumptions, using the analysis in [8], the expected nonlinear elastic and viscous Fourier–Tschebyshev coefficients and the nonlinear viscous Fourier–Tschebyshev coefficients are given by

$$e_1 \equiv G_1' = G_0 + \frac{3}{4}\left(\frac{\gamma_0}{\gamma^*}\right)^2 G_\beta(t), \tag{53a}$$

$$e_3 \equiv -G_3' = \frac{1}{4}\left(\frac{\gamma_0}{\gamma^*}\right)^2 G_\beta(t), \tag{53b}$$

$$v_1 \equiv \frac{G_1''}{\omega} = \eta_0 - \frac{3}{4}\left(\frac{\dot{\gamma}_0}{\dot{\gamma}^*}\right)^2 \eta_\beta, \tag{53c}$$

$$v_3 \equiv \frac{G_3''}{\omega} = -\frac{1}{4}\left(\frac{\dot{\gamma}_0}{\dot{\gamma}^*}\right)^2 \eta_\beta, \tag{53d}$$

where $G_\beta(t)$ is specified above. Again motivated by the data in Fig. 9 and 10, we select the following parameter values: $G_0 = 5$ Pa, $\gamma^* = 2$, $\eta_0 = 7$ Pa s, $\eta_\beta = 3$ Pa s, $\dot{\gamma}^* = 3\ \mathrm{s}^{-1}$, and $c_0 = 4$ Pa. We can now vary the thixotropic parameter τ_{thix} to explore how the rate of mutation of the material properties influences the measurement error in the nonlinear Fourier–Tschebyshev coefficients determined using the Gaborheometry technique. The resulting parameter space is large because of the number of material coefficients that must be determined to fully characterize the nonlinear material response. Here, we focus on the error in the first elastic coefficient $e_1(\gamma)$ for various values of the material mutation number (characterizing the rate of change) and various dimensionless values of the ramp rate describing the amplitude-modulated signal [Eq. (42)]. In order to systematically compute a measure of the errors incurred by the evolving material properties and the increasing strain amplitude, we reference the error in the measured e_1 for a given strain amplitude w.r.t $e_1(\gamma_0, t = 0)$, i.e., the value of the elastic modulus for a given strain amplitude at $t = 0$ is considered here as the correct or expected property. Therefore, the mutation time of the property $e_1(\gamma_0)$ which is the characteristic time for the change of the material property is given as

$$\lambda_{Mu} = \left[\frac{1}{e_1}\frac{\Delta e_1}{\Delta t}\right]^{-1}, \tag{54}$$

where Δe_1 is the change in property e_1 from its initial state and Δt is the time taken for the imposed strain ramp to achieve this change in the property. The experimental time taken to measure the data point of interest using the discrete Gabor transform is Δt as well. Therefore, the mutation number for e_1 for this toy model is

$$Mu_{\text{material}} \equiv Mu_{e_1} = \frac{\Delta e_1}{e_1(\gamma_0)}. \tag{55}$$

We choose an amplitude-modulated signal of the form $\gamma(t) = (\gamma_i + rt)\sin(\omega t)$ where $\gamma_i = 0.01$ to demonstrate the potential of amplitude-modulated (AM) sweeps for LAOS in mutating materials. The ramp-rate is $r = 0.3$ and the timescale τ_{thix} in G_β is varied in order to simulate the error incurred in determining e_1 for a range of mutation numbers of the material [Eq. (55)] and a range of amplitude mutation numbers [Eq. (42)] while using our discrete Gabor transform amplitude sweep technique. In Fig. 15 we show a contour plot of the percentage error incurred by determining the value of e_1 for various values of Mu_{material} and for a range of amplitude mutation numbers (Mu_{amp}). Please note that in our calculation for Mu_{material} in Fig. 15, only the time dependent part of e_1 is considered. Similar contour plots can also be made for the error in $e_3(t)$ as well. It is evident that as the material mutation number and the ramp rate each decrease towards zero, we obtain increasingly accurate values of e_1.

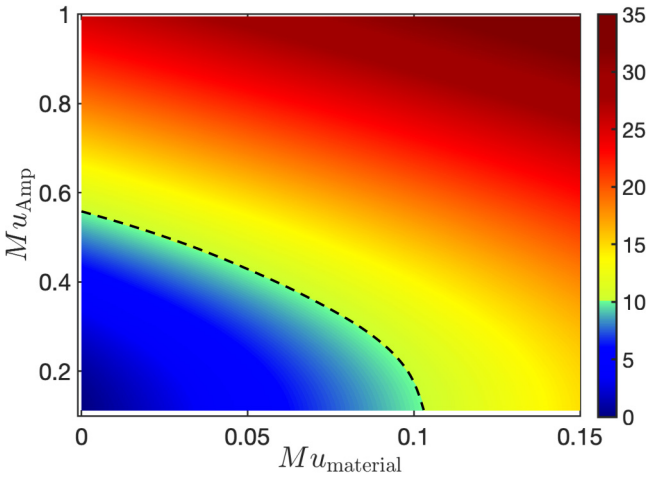

FIG. 15. Contour plot showing the percentage error incurred in determining values of the first Tschebyshev coefficient e_1 for the nonlinear Kelvin–Voigt model at various values of Mu_{material} [Eq. (2)] and Mu_{Amp} [Eq. (42)]. The area bounded by the dashed line (corresponding to a 10% error contour) indicates an appropriate operability window for using the DGT in conjunction with amplitude-modulated ramps to measure the weakly nonlinear properties of a mutating material.

The dashed line in Fig. 15 shows the contour line corresponding to a percentage error of 10%. The blue shaded area bounded by the contour line indicates the operability window within which we can safely use the discrete Gabor transform technique described in this paper to obtain the nonlinear Fourier–Tschebyshev coefficients even for a mutating or time-evolving material.

V. SUMMARY AND FUTURE OUTLOOK

In this paper, we have shown how the discrete Gabor transform—a special case of the STFT with a Gaussian window specified by its parameter a—can provide time resolution to the determination of viscoelastic material properties in nonergodic systems. Important implementation details such as the need for appropriate amplitude correction and optimal window length selection have been discussed in order to enable us to use the discrete Gabor transform techniques for quantitative rheometry. An important criterion while processing recorded oscillatory data using this discrete transform technique is periodicity. Periodicity of the time signal must be ensured before using the discrete Fourier transform or discrete Gabor transform to avoid spectral leakage. This can be ensured using a suitable window function $w(t)$. In Sec. III C, we also showed that the optimal window length selection is given by $4a = 1.68(2\pi/\omega_i) = 10.56/\omega_i$ or equivalently $a\omega_i = 2.63$ in order to obtain optimal time and frequency resolution, where ω_i is the lowest frequency present in a general multiwave input signal. In conventional SAOS rheometry this is the single input frequency. We showed that decreasing the window length in an attempt to increase the time resolution can lead to significant oscillatory error with the periodic fluctuations occurring at twice the frequency of the input time signal. To obtain further improvements in the time resolution, one potential option is to use a shorter window length, below

$4a = 1.68(2\pi/\omega_i)$ and then pass the output of the discrete Gabor transform through a low-pass filter with cutoff frequency less than $2\omega_i$ in order to filter out the oscillatory component of the output error. Care of course must be exercised here to ensure the amplitude and phase of the filtered signal is preserved (or corrected) or the computed values of the complex modulus will be in error.

The constraints on the values of $a\omega_i$ proposed in the present paper provide a guideline for selecting the temporal window length based on the imposed frequency of deformation (which is known *a priori*) to obtain optimal time-frequency resolution. Importantly, the test signal frequency remains constant throughout a typical rheometric experiment. The material mutation time scale λ_{Mu} is, however, not known *a priori*. From our computational experiments with time-evolving models (in which the ground truth is known), we have determined that we need to ensure that the mutation number is $Mu_{Amp} \leq 0.1$ to achieve sufficient accuracy in measuring the material functions and extracting the mutation time-scale of a thixotropic material. In the future, it is possible to imagine a "smart" or data-informed adaptive Gaborheometry technique that monitors the rate of sample mutation extracted by repeated Gabor transforms of the output signal in real time and adjusts the oscillatory test frequency imposed by the rheometer to satisfy this constraint.

The applications of the discrete Gabor transform in rheometry that have been demonstrated in the present paper include (i) extracting time-dependent linear viscoelastic complex moduli for mutating materials; (ii) extracting both the initial transient and ultimate steady state oscillatory response from the start-up of oscillatory shear flow; (iii) obtaining the dependence of the nonlinear elastic and viscous Fourier–Tschebyshev coefficients on strain amplitude for a specified frequency ω_i by using an amplitude-modulated (AM) signal given by Eq. (39) to perform a slow strain ramp. We use this latter analysis to provide an operability diagram for using such AM signals on weakly mutating materials.

Using this relatively straightforward Gaborheometry protocol it is possible to extract accurate time- and strain-resolved properties of complex fluids and soft solids even as they undergo rheological aging. Importantly, this analysis can be done offline and does not require any special input sequence or deformation wave-form (except for the continuously ramped strain amplitude described in Sec. IV C). It can, thus, be applied as a postprocessing step to any previously recorded deformation history [provided the full vectors of $\gamma(t)$ and $\sigma(t)$ have been digitized and recorded for $0 < t < T$]. This technique can be extended to other (non-Gaussian) window functions as well. However, we have selected to focus exclusively on Gaussian windows in the current paper since it can be shown that they provide the best (optimal) time-frequency resolution [56]. We hope this relative ease of implementation will promote broad adoption of Gaborheometry for thixotropic and aging viscoelastic materials in the future.

ACKNOWLEDGMENTS

J.D.J.R. would like to thank Aramco Americas for the financial support of his studies into mutating materials. The authors are grateful for the fruitful discussions with Professor James W. Swan, Dr. Ashok Santra, Dr. Miguel Gonzalez, and Kyle Lennon.

AUTHOR DECLARATIONS

Conflict of Interest

The authors have no conflicts to disclose.

DATA AVAILABILITY

The data that support the findings of this study are available from the corresponding author upon reasonable request.

APPENDIX A: TIME FREQUENCY UNCERTAINTY

When using the STFT technique, there is always a trade-off between frequency and time resolution. Longer windows give better frequency resolution but poorer time resolution, whereas shorter windows provide better time resolution but poor frequency resolution. The time-frequency spread around a Gaussian operator $g(t)$ obeys the Heisenberg uncertainty principle [58,59]

$$\left(\int_{-\infty}^{\infty} t^2 |g(t)|^2 dt\right)\left(\int_{-\infty}^{\infty} \omega^2 |\tilde{g}(\omega)|^2 d\omega\right) \geq \frac{1}{16\pi^2}. \quad \text{(A1)}$$

The kernel inside the time integral is the variance of the time signal $g(t)$ and the kernel inside the frequency integral is the variance of $\tilde{g}(\omega)$, which is the Fourier transform of $g(t)$ in frequency space. For a Gaussian time signal, the output of the Fourier transform also results in a Gaussian function $\tilde{g}(\omega)$.

To illustrate this time-frequency uncertainty principle, we consider the signal discussed in Sec II B,

$$x(t) = \begin{cases} \sin(1t), & t < 15\pi \text{ s}, \\ \sin(5t), & t \geq 15\pi \text{ s}. \end{cases} \quad \text{(A2)}$$

The input signal, thus, changes abruptly from $\omega_i = 1$ to $\omega_i = 5$ rad/s at $t = 15\pi$. The initial frequency $\omega_i = 1$ rad/s is the smallest and thus constrains the time resolution. We sample this signal with $N = 20\,480$ points at a sampling frequency of 217 samples per second (dt = 0.0046 s).

The DGT amplitude spectrum of Eq. (A2) for two different window lengths [$4a = 1.68(2\pi/\omega_i) = 10.56$ s and $4a = 16.8(2\pi/\omega_i) = 10.56$ s] are shown in Fig. 16. We define $\Delta\omega$ (i.e., the characteristic frequency resolution) to be the range of discrete frequencies around the given signal frequency for which the computed power in the frequency spectrum is more than 80% of the amplitude spectrum at the input signal frequency ω_i. Note that the contribution of these additional frequencies around the specified input frequency of the signal arises purely from windowing as illustrated in Fig. 7(b). We define Δt to be the time resolution with which we resolve the step change in the

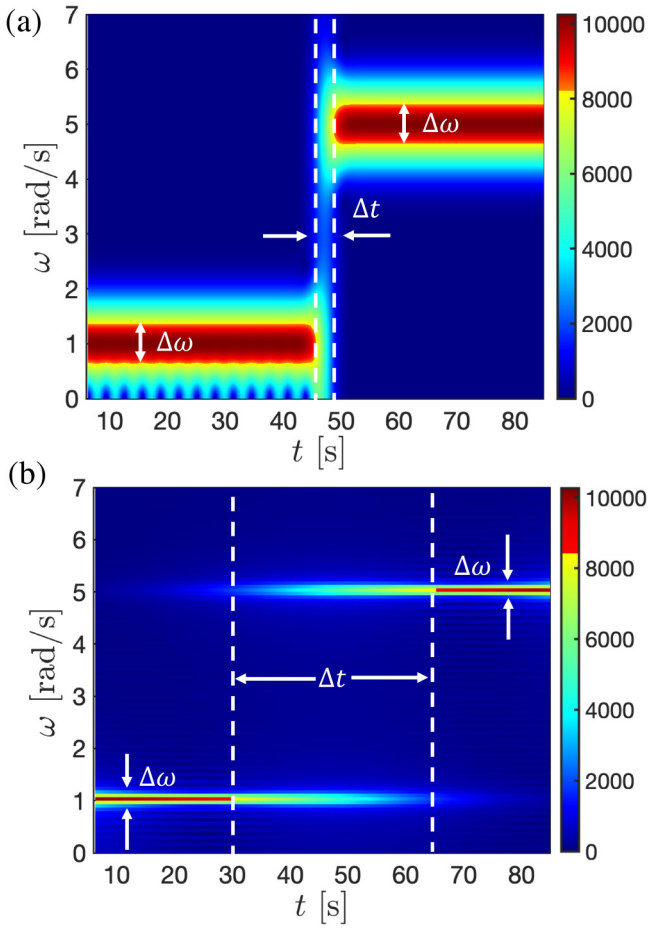

FIG. 16. (a) DGT spectrum of Eq. (A2) with $a = 2.63$ s. (b) DGT spectrum of Eq. (A2) with $a = 26.3$ s. The total number of points and the sampling time interval for both cases are $N = 20\,480$ and $dt = 0.0046$ s. As the time resolution increases, the frequency resolution decreases and vice versa.

frequency of the input signal at $t = 15\pi$. More specifically, we identify Δt to be the time it takes to undergo 80% of the amplitude change in the Heaviside step function embodied by Eq. (A2). It can be seen from Fig. 16 that for a shorter window length $4a = 1.68(2\pi/\omega_i) = 10.56$ s ($a\omega_i = 2.63$), Δt is smaller and the time resolution is better than for the longer window length $4a = 16.8(2\pi/\omega_i) = 105.6$ s ($a\omega_i = 26.3$). However, this results in the frequency resolution $\Delta\omega$ becoming poorer compared to the wider window. This illustrates graphically the trade-off in time and frequency resolution embodied in the time-frequency uncertainty principle.

APPENDIX B: RESOLUTION AND ACCURACY OF RECTANGULAR AND GAUSSIAN WINDOW

Here, we compare the performance of a piece-wise rectangular window (which is implemented in some advanced rheometer software as a "fast sampling" mode) with the Gaussian window that is employed in the Gabor transform. To enable a careful comparison of the errors incurred by windowing, we consider a Kelvin–Voigt model similar to Eq. (26) but with a nonlinear time-dependent elastic modulus and a constant (time-invariant) viscous contribution

$$\sigma(t) = E(t)\gamma(t) + \eta_0\dot{\gamma}, \tag{B1}$$

where

$$E(t) = 10 + 0.5t^{1.5}, \tag{B2}$$

with t in seconds, $E(t)$ in Pascals, and $\eta_0 = 2$ Pa s. For this model, the analytical expression for the storage and loss modulus are given by $G'(\omega, t) = 10 + 0.5t^{1.5}$ and $G''(\omega) = \eta_0\omega$. Selecting an input frequency of $\omega_i = 10$ rad/s, we can calculate the storage modulus and the loss modulus using Eq. (25) from both piece-wise rectangular windows of different window lengths as well as using Gaussian windows of different window lengths (determined by the product $a\omega_i$). For a piece-wise rectangular window, the length of the nonzero portion of the window function is the relevant measure of its size. For a Gaussian window, we take the value of $4a$ in Eq. (9) as the measure of the window length. We define the error incurred by the STFT calculation from the different windows to be

$$\text{Error} = \frac{1}{N}\sum_{n=1}^{N}\left(\left|\log_{10}\left(G'_{\text{STFT}}(t_n)/G'_{\text{analytical}}(t_n)\right)\right| + \left|\log_{10}\left(G''_{\text{STFT}}(t_n)/G''_{\text{analytical}}(t_n)\right)\right|\right). \tag{B3}$$

The error from the STFT calculations using Eq. (25) for different lengths of both the rectangular window and the Gaussian window is illustrated in Fig. 17. From Fig. 17, we note that the Gaussian window resolves the time-dependent evolution of the signal with a smaller error than the rectangular window for any value of window width. We can also note that the minimum error is observed for a Gaussian window with a width between $1 \leq 4a/(2\pi/\omega_i) \leq 2$. Additional exploratory calculations show that the span of this minimum error interval is also dependent on the specific form of the time-dependency (i.e., on the mutation number based on the discussion in Sec. IV D) as well as the different frequencies present in a time and strain-dependent

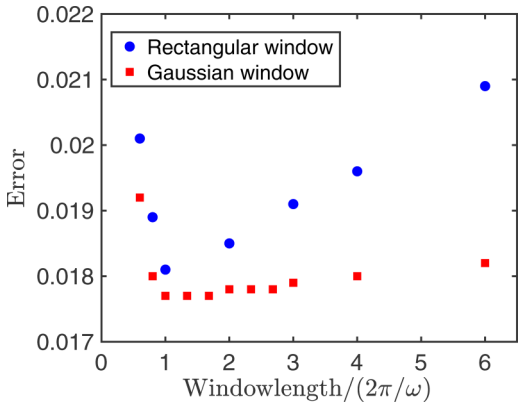

FIG. 17. Comparison of the error defined in Eq. (B3) for the nonlinear aging Kelvin–Voigt model given in Appendix B using rectangular windows and Gaussian windows of different window lengths.

nonlinear signal. However, it is also evident from Fig. 17 that this local minimum is quite broad so the precise value of $a\omega_i$ selected is not critical. In general we recommend a window length of $4a = 1.68 \cdot (2\pi/\omega_i)$ s ($a\omega_i = 2.63$) for standard rheological experiments.

REFERENCES

[1] Daugman, J. G., "Complete discrete 2-D Gabor transforms by neural networks for image analysis and compression," IEEE Trans. Acoust., Speech., Signal. Process. **36**, 1169–1179 (1988).

[2] Donoho, D. L., M. Vetterli, R. A. DeVore, and I. Daubechies, "Data compression and harmonic analysis," IEEE Trans. Inf. Theory **44**, 2435–2476 (1998).

[3] Feichtinger, H. G., and T. Strohmer, *Gabor Analysis and Algorithms: Theory and Applications* (Springer Science & Business Media, New York, 2012).

[4] Hansen, F. K., K. M. Gorski, and E. Hivon, "Gabor transforms on the sphere with applications to CMB power spectrum estimation," Mon. Not. R. Astron. Soc. **336**, 1304–1328 (2002).

[5] Yao, J., P. Krolak, and C. Steele, "The generalized Gabor transform," IEEE Trans. Image Process. **4**, 978–988 (1995).

[6] Lahmiri, S., and M. Boukadoum, "Hybrid discrete wavelet transform and Gabor filter banks processing for features extraction from biomedical images," J. Med. Eng. **2013**, 104684 (2013).

[7] Suzuki, H., T. Kinjo, Y. Hayashi, M. Takemoto, and K. Ono, "Wavelet transform of acoustic emission signals," Journal of Acoustic Emission **14**, 69–84 (1996).

[8] Ewoldt, R. H., "Defining nonlinear rheological material functions for oscillatory shear," J. Rheol. **57**(1), 177–195 (2013).

[9] Ewoldt, R. H., P. Winter, J. Maxey, and G. H. McKinley, "Large amplitude oscillatory shear of pseudoplastic and elastoviscoplastic materials," Rheol. Acta **49**, 191–212 (2010).

[10] Ewoldt, R. H., and N. A. Bharadwaj, "Low-dimensional intrinsic material functions for nonlinear viscoelasticity," Rheol. Acta **52**(3), 201–219 (2013).

[11] Ewoldt, R. H., A. E. Hosoi, and G. H. McKinley, "New measures for characterizing nonlinear viscoelasticity in large amplitude oscillatory shear," J. Rheol. **52**, 1427–1458 (2008).

[12] Ewoldt, R. H., A. E. Hosoi, and G. H. McKinley, "Nonlinear viscoelastic biomaterials: Meaningful characterization and engineering inspiration," Integr. Comp. Biol. **49**, 40–50 (2009).

[13] Ewoldt, R. H., C. Clasen, A. E. Hosoi, and G. H. McKinley, "Rheological fingerprinting of gastropod pedal mucus and synthetic complex fluids for biomimicking adhesive locomotion," Soft Matter **3**, 634–643 (2007).

[14] Dimitriou, C. J., R. H. Ewoldt, and G. H. McKinley, "Describing and prescribing the constitutive response of yield stress fluids using large amplitude oscillatory shear stress (LAOStress)," J. Rheol. **57**, 27–70 (2013).

[15] Ng, T. S. K., G. H. McKinley, and R. H. Ewoldt, "Large amplitude oscillatory shear flow of gluten dough: A model power-law gel," J. Rheol. **55**, 627–654 (2011).

[16] Hyun, K., M. Wilhelm, C. O. Klein, K. S. Cho, J. G. Nam, K. H. Ahn, S. J. Lee, R. H. Ewoldt, and G. H. McKinley, "A review of nonlinear oscillatory shear tests: Analysis and application of large amplitude oscillatory shear (LAOS)," Prog. Polym. Sci. **36**, 1697–1753 (2011).

[17] Singh, P. K., J. M. Soulages, and R. H. Ewoldt, "Frequency-sweep medium-amplitude oscillatory shear (MAOS)," J. Rheol. **62**, 277–293 (2017).

[18] Martinetti, L., and R. H. Ewoldt, "Time-strain separability in medium-amplitude oscillatory shear," Phys. Fluids **31**(2), 021213 (2019).

[19] Rogers, S. A., B. M. Erwin, D. Vlassopoulos, and M. Cloitre, "A sequence of physical processes determined and quantified in LAOS: Application to a yield stress fluid," J. Rheol. **55**(2), 435–458 (2011).

[20] Erturk, M. Y., S. A. Rogers, and J. Kokini, "Comparison of sequence of physical processes (SPP) and fourier transform coupled with Chebyshev polynomials (FTC) methods to interpret large amplitude oscillatory shear (LAOS) response of viscoelastic doughs and viscous pectin solution," Food Hydrocolloids **128**, 107558 (2022).

[21] Lennon, K. R., G. H. McKinley, and J. W. Swan, "Medium amplitude parallel superposition (MAPS) rheology. Part 1: Mathematical framework and theoretical examples," J. Rheol. **64**(3), 551–579 (2020).

[22] Lennon, K. R., M. Geri, G. H. McKinley, and J. W. Swan, "Medium amplitude parallel superposition (MAPS) rheology. Part 2: Experimental protocols and data analysis," J. Rheol. **64**, 1263–1293 (2020).

[23] Rathinaraj, J. D. J., G. H. McKinley, and B. Keshavarz, "Incorporating rheological nonlinearity into fractional calculus descriptions of fractal matter and multi-scale complex fluids," Fractal Fractional **5**(4), 174 (2021).

[24] Jaishankar, A., and G. H. McKinley, "A fractional K-BKZ constitutive formulation for describing the nonlinear rheology of multiscale complex fluids," J. Rheol. **58**, 1751–1788 (2014).

[25] Holten-Andersen, N., M. J. Harrington, H. Birkedal, B. P. Lee, P. B. Messersmith, K. Y. C. Lee, and J. H. Waite, "pH-induced metal-ligand cross-links inspired by mussel yield self-healing polymer networks with near-covalent elastic moduli," Proc. Natl. Acad. Sci. U.S.A. **108**, 2651–2655 (2011).

[26] Li, H., P. Yang, P. Pageni, and C. Tang, "Recent advances in metal-containing polymer hydrogels," Macromol. Rapid Commun. **38**(14), 1700109 (2017).

[27] Mewis, J., "Thixotropy—A general review," J. Non-Newtonian Fluid Mech. **6**, 1–20 (1979).

[28] Mewis, J., and N. J. Wagner, "Thixotropy," Adv. Colloid Interface Sci. **147–148**, 214–227 (2009).

[29] Larson, R. G., and Y. Wei, "A review of thixotropy and its rheological modeling," J. Rheol. **63**, 477–501 (2019).

[30] Dullaert, K., and J. Mewis, "Thixotropy: Build-up and breakdown curves during flow," J. Rheol. **49**, 1213–1230 (2005).

[31] Joshi, Y. M., and G. R. K. Reddy, "Aging in a colloidal glass in creep flow: Time-stress superposition," Phys. Rev. E **77**, 021501 (2008).

[32] Joshi, Y. M., "Dynamics of colloidal glasses and gels," Annu. Rev. Chem. Biomol. Eng. **5**(1), 181–202 (2014).

[33] Joshi, Y. M., G. K. Reddy, A. L. Kulkarni, N. Kumar, and R. P. Chhabra, "Rheological behaviour of aqueous suspensions of laponite: New insights into the ageing phenomena," Proc. R. Soc. A. **464**, 469–489 (2008).

[34] Awasthi, V., and Y. M. Joshi, "Effect of temperature on aging and time-temperature superposition in nonergodic laponite suspensions," Soft Matter **5**(24), 4991–4996 (2009).

[35] Baldewa, B., and Y. M. Joshi, "Thixotropy and physical aging in acrylic emulsion paint," Polym. Eng. Sci. **51**(10), 2085–2092 (2011).

[36] Kaushal, M., and Y. M. Joshi, "Linear viscoelasticity of soft glassy materials," Soft Matter **10**(12), 1891–1894 (2014).

[37] Shahin, A., and Y. M. Joshi, "Hyper-aging dynamics of nanoclay suspension," Langmuir **28**, 5826–5833 (2012).

[38] Shahin, A., and Y. M. Joshi, "Irreversible aging dynamics and generic phase behavior of aqueous suspensions of laponite," Langmuir **26**, 4219–4225 (2010).

[39] Shahin, A., and Y. M. Joshi, "Physicochemical effects in aging aqueous laponite suspensions," Langmuir **28**, 15674–15686 (2012).

[40] Shahin, A., and Y. M. Joshi, "Prediction of long and short time rheological behavior in soft glassy materials," Phys. Rev. Lett. **106**, 038302 (2011).

[41] Shukla, A., S. Shanbhag, and Y. M. Joshi, "Analysis of linear viscoelasticity of aging soft glasses," J. Rheol. **64**, 1197–1207 (2020).

[42] Agarwal, M., and Y. M. Joshi, "Signatures of physical aging and thixotropy in aqueous dispersion of Carbopol," Phys. Fluids **31**, 063107 (2019).

[43] Bandyopadhyay, R., P. Harsha Mohan, and Y. M. Joshi, "Stress relaxation in aging soft colloidal glasses," Soft Matter **6**(7), 1462–1466 (2010).

[44] Gupta, R., B. Baldewa, and Y. M. Joshi, "Time temperature superposition in soft glassy materials," Soft Matter **8**(15), 4171–4176 (2012).

[45] Mours, M., and H. H. Winter, "Time-resolved rheometry," Rheol. Acta **33**(5), 385–397 (1994).

[46] Curtis, D. J., A. Holder, N. Badiei, J. Claypole, M. Walters, B. Thomas, M. Barrow, D. Deganello, M. R. Brown, P. R. Williams, and K. Hawkins, "Validation of optimal fourier rheometry for rapidly gelling materials and its application in the study of collagen gelation," J. Non-Newtonian Fluid Mech. **222**, 253–259 (2015).

[47] Coussot, P., H. Tabuteau, X. Chateau, L. Tocquer, and G. Ovarlez, "Aging and solid or liquid behavior in pastes," J. Rheol. **50**, 975–994 (2006).

[48] Winter, H. H., and F. Chambon, "Analysis of linear viscoelasticity of a crosslinking polymer at the gel point," J. Rheol. **30**, 367–382 (1986).

[49] Geri, M., B. Keshavarz, T. Divoux, C. Clasen, D. J. Curtis, and G. H. McKinley, "Time-resolved mechanical spectroscopy of soft materials via optimally windowed chirps," Phys. Rev. X **8**, 041042 (2018).

[50] Bouzid, M., B. Keshavarz, M. Geri, T. Divoux, E. Del Gado, and G. H. McKinley, "Computing the linear viscoelastic properties of soft gels using an optimally windowed chirp protocol," J. Rheol. **62**, 1037–1050 (2018).

[51] Ghiringhelli, E., D. Roux, D. Bleses, H. Galliard, and F. Caton, "Optimal fourier rheometry: Application to the gelation of an alginate," Rheol. Acta **51**, 413–420 (2012).

[52] Rathinaraj, J. D. J., J. Hendricks, G. H. McKinley, and C. Clasen, "Orthochirp: A fast spectro-mechanical probe for monitoring transient microstructural evolution of complex fluids during shear," J. Non-Newtonian Fluid Mech. **301**, 104744 (2022).

[53] Keshavarz, B., D. G. Rodrigues, J.-B. Champenois, M. G. Frith, J. Ilavsky, M. Geri, T. Divoux, G. H. McKinley, and A. Poulesquen, "Time–connectivity superposition and the gel/glass duality of weak colloidal gels," Proc. Natl. Acad. Sci. U.S.A. **118**(15), e2022339118 (2021).

[54] Tassieri, M., M. Laurati, D. J. Curtis, D. W. Auhl, S. Coppola, A. Scalfati, K. Hawkins, P. R. Williams, and J. M. Cooper, "i-Rheo: Measuring the materials' linear viscoelastic properties 'in a step'!," J. Rheol. **60**(4), 649–660 (2016).

[55] Wang, F.-W., M. Geri, Y.-J. Chen, J.-R. Huang, G. H. McKinley, and Y.-L. Chen, "Rheo-chemistry of gelation in aiyu (fig) jelly," Food Hydrocolloids **123**, 107001 (2022).

[56] Gabor, D., "Theory of communication. Part 1: The analysis of information," J. Inst. of Electr. Eng.,-Part III **93**(26), 429–441 (1946).

[57] Capus, C., and K. Brown, "Short-time fractional Fourier methods for the time-frequency representation of chirp signals," J. Acoust. Soc. Am. **113**(6), 3253–3263 (2003).

[58] Kutz, J. N., *Data-Driven Modeling & Scientific Computation: Methods for Complex Systems & Big Data* (Oxford University Press, Oxford, 2013).

[59] Brunton, S. L., and J. N. Kutz, *Data-Driven Science and Engineering: Machine Learning, Dynamical Systems, and Control* (Cambridge University Press, Cambridge, 2019).

[60] Bird, R. B., and A. J. Giacomin, "Who conceived the 'complex viscosity'?," Rheol. Acta **51**(6), 481–486 (2012).

[61] Smith, J. O., *Mathematics of the Discrete Fourier Transform (DFT): With Audio Applications* (BookSurge, Charleston, 2007).

[62] Sejdić, E., I. Djurović, and J. Jiang, "Time–frequency feature representation using energy concentration: An overview of recent advances," Digital Signal Process. **19**(1), 153–183 (2009).

[63] Brandt, A., *Noise and Vibration Analysis: Signal Analysis and Experimental Procedures* (John Wiley & Sons, Chichester, 2011).

[64] van Dusschoten, D., and M. Wilhelm, "Increased torque transducer sensitivity via oversampling," Rheol. Acta **40**(4), 395–399 (2001).

[65] Lee, J. C.-W., Y.-T. Hong, K. M. Weigandt, E. G. Kelley, H. Kong, and S. A. Rogers, "Strain shifts under stress-controlled oscillatory shearing in theoretical, experimental, and structural perspectives: Application to probing zero-shear viscosity," J. Rheol. **63**, 863–881 (2019).

[66] Hassager, O., "Stress-controlled oscillatory flow initiated at time zero: A linear viscoelastic analysis," J. Rheol. **64**, 545–550 (2020).

[67] Wagner, M. H., and J. Meissner, "Network disentanglement and time-dependent flow behaviour of polymer melts," Die Makromolekulare Chemie **181**(7), 1533–1550 (1980).

[68] Rathinaraj, J. D. J., B. Keshavarz, and G. H. McKinley, "Why the Cox–Merz rule and Gleissle mirror relation work: A quantitative analysis using the Wagner integral framework with a fractional Maxwell kernel," Phys. Fluids **34**(3), 033106 (2022).